JBC RESEARCH ARTICLE

Crystal structures of *Schistosoma mansoni* histone deacetylase 8 reveal a novel binding site for allosteric inhibitors

Received for publication, June 9, 2022, and in revised form, August 10, 2022 Published, Papers in Press, August 13, 2022,
https://doi.org/10.1016/j.jbc.2022.102375

Fulvio Saccoccia[1,*], Luca Pozzetti[2], Roberto Gimmelli[1], Stefania Butini[2], Alessandra Guidi[1], Giuliana Papoff[1], Marialaura Giannaccari[1], Simone Brogi[3], Viviana Scognamiglio[4], Sandra Gemma[2], Giovina Ruberti[1,*,‡], and Giuseppe Campiani[2,*,‡]

From the [1]Institute of Biochemistry and Cell Biology, Italian National Research Council (IBBC-CNR), Adriano Buzzati-Traverso Campus, Monterotondo Scalo, Rome, Italy; [2]Department of Biotechnology, Chemistry and Pharmacy, DoE Department of Excellence 2018-2022, University of Siena, Siena, Italy; [3]Department of Pharmacy, University of Pisa, Pisa, Italy; [4]Institute of Crystallography, Italian National Research Council, Department of Chemical Sciences and Materials Technologies, Monterotondo, Italy

Edited by Joseph Jez

Parasitic diseases cause significant global morbidity and mortality particularly in the poorest regions of the world. Schistosomiasis, one of the most widespread neglected tropical diseases, affects more than 200 million people worldwide. Histone deacetylase (HDAC) inhibitors are prominent epigenetic drugs that are being investigated in the treatment of several diseases, including cancers and parasitic diseases. *Schistosoma mansoni* HDAC8 (*Sm*HDAC8) is highly expressed in all life cycle stages of the parasite, and selective inhibition is required in order to avoid undesirable off-target effects in the host. Herein, by X-ray crystal structures of *Sm*HDAC8-inhibitor complexes, biochemical and phenotypic studies, we found two schistosomicidal spiroindoline derivatives binding a novel site, next to Trp198, on the enzyme surface. We determined that by acting on this site, either by mutation of the Trp198 or by compound binding, a decrease in the activity of the enzyme is achieved. Remarkably, this allosteric site differs from the human counterpart; rather, it is conserved in all *Schistosoma* species, as well as Rhabidoptera and Trematoda classes, thus paving the way for the design of HDAC8-selective allosteric inhibitors with improved properties.

Control of schistosomiasis is of global medical and veterinary importance for the World Health Organization 2021 to 2030 neglected tropical disease road map (https://www.who.int/publications/i/item/9789240010352). Schistosomiasis is a chronic and debilitating disease, caused by the parasitic trematodes of the genus *Schistosoma*. It is spread worldwide in tropical and subtropical areas, and it affects more than 200 million people with the greatest human burden within sub-Saharan Africa. Three main species of schistosomes infect humans, namely *Schistosoma haematobium*, *Schistosoma mansoni*, and *Schistosoma japonicum*. Schistosomes have a complex life cycle and develop in the intermediate freshwater snail hosts and in mammalian definitive hosts, such as humans, through several different morphological stages. The pathology occurs mainly from the parasite eggs trapped in the host tissues that cause host immune response and severe granulomatous reactions (1). Nowadays, praziquantel (PZQ) is the drug of choice in the treatment of schistosomiasis; however, it is not effective on juvenile parasites and it does not prevent reinfection (2). Various combinations of *Schistosoma* species (spp) hybrids have been documented within snails, livestock, wildlife, and within humans and their sensitivity to PZQ is still poorly investigated (3). Moreover, for its massive and widespread use, the possible occurrence of drug resistance to PZQ is an ever-present threat. Overall, the social and economic burden due to schistosomiasis is very high and novel drugs for prevention and treatment besides sanitation are required.

Promising drug targets in *Schistosoma*, as in other parasites, are histone deacetylase (HDAC) enzymes, members of an evolutionarily ancient enzyme family that regulate the activity of their substrates by removing acetyl groups from lysine residues. Lysine acetylation is one of the major post-translational protein modifications playing strategic roles in cell signaling, cell cycle control, and in epigenetic regulation of gene expression (4). Due to the poor selectivity and undesirable side effects that occur with pan-inhibitors, the development of selective inhibitors has attracted the attention of several investigators.

S. mansoni expresses several HDACs and among them HDAC8, a class I HDAC, particularly abundant in all stages of the parasite life cycle and poorly expressed in healthy human tissues, is largely recognized as a promising therapeutic target (5, 6). Class I HDACs (HDAC1-3 and HDAC8) are highly regulated. HDAC8, located both in the nucleus and in the

‡ These authors contributed equally to this work.
* For correspondence: Fulvio Saccoccia, fulvio.saccoccia@cnr.it; Giovina Ruberti, giovina.ruberti@cnr.it; Giuseppe Campiani, campiani@unisi.it.
Present address for Alessandra Guidi: Institute of Molecular Biology and Pathology, Italian National Research Council (IBPM-CNR), c/o Department of Biology and Biotechnology "Charles Darwin", Sapienza University of Rome, P. le Aldo Moro 5, 00,185 Roma, Italy.

cytosol, is the only one acting as a monomer, while all other Class I HDACs work as components of multiprotein complexes, opening the challenging possibility to get isoform selectivity through the design of inhibitors of individual complexes (7). Human HDAC1-3 enzymatic activity could be also positively modulated by inositol phosphates through an allosteric communication between the inositol-binding site and the catalytic site (8). Recently, a region mapping to α1-loop1-α2 has been identified as an allosteric site in human HDAC8 (9). A better knowledge of the mechanisms regulating the enzymatic activity and a deeper knowledge of the structure of each HDAC isoform can be instrumental for the design of selective inhibitors.

*Sm*HDAC8 is a metal-dependent enzyme, harboring a zinc ion in the active site, and, so far, the vast majority of discovered inhibitors present a zinc-binding group, such as a hydroxamate or a sulfur moiety (10). Specificity toward different HDAC isoforms may be obtained by an appropriately designed linker and cap groups or by exploiting specific and unique regulatory sites. Through a concerted effort involving molecular modeling, phenotypic screening, and enzymatic inhibition assays of *Sm*HDAC8 enzyme, we previously identified novel HDAC inhibitors as promising multistage antischistosomicidal hits (11). The most interesting scaffold presented a thieno[3,2-b]indole (compound NF2624) or a spiro-indoline (compounds NF2453, NF2452) core moieties coupled to a hydroxamate-based zinc-binding group ((11), Fig. 1). Based on our previous results, we investigated the structure–activity relationships of both scaffolds, developing new inhibitors. X-ray complexes structures as well as biochemical and phenotypic assays were crucial to characterize the binding mode and activity of the novel NF2886, NF2883, and NF2889 and the former NF2624. We successfully solved the X-ray crystal structures of *Sm*HDAC8 in complex with all of the four analogs, representative of both classes of compounds. Remarkably, we discovered that the spiroindoline derivatives, NF2883 and NF2889, bind a specific site different from the catalytic site, in the vicinity of Trp198 on the enzyme surface, and inhibit the enzyme in a mixed/allosteric manner. Multiple sequence alignment shows differences at this site in *S. mansoni* and human HDAC8. Phylogeny studies reveal that this site is conserved in all *Schistosoma* spp, paving the way for the discovery of selective *Sm*HDAC8 inhibitors, and in other members of the Trematoda phylum, opening the possibility to identify compounds active toward several pathogenic parasites.

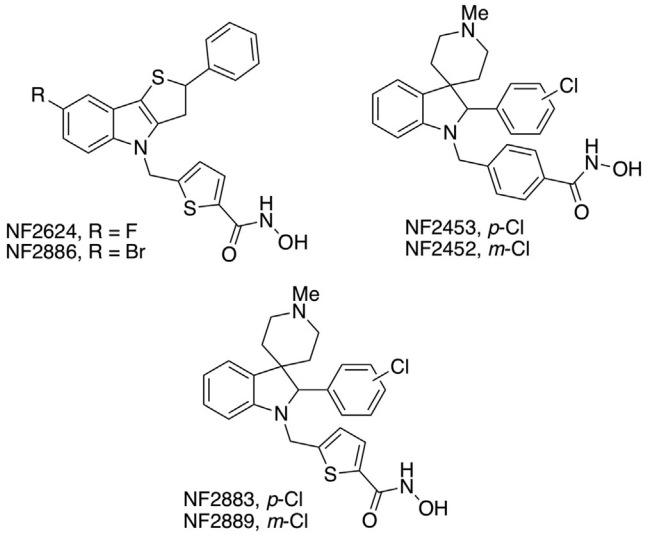

Figure 1. Structures of the thieno[3,2-b]indole and spiroindoline derivatives HDAC inhibitors investigated in the present work.

Results

We have recently identified through virtual screening and phenotypical studies of selected hits, novel HDAC inhibitors characterized by the presence of a hydroxamate-based metal-binding group coupled to a tricyclic thieno[3,2-b]indole or a spiro-indoline core as capping groups able to impair viability of larval, juvenile, and adult *S. mansoni* and inhibiting *Sm*HDAC8 recombinant protein activity *in vitro* (11). Among the previously identified class of inhibitors, we designed novel molecules in order to investigate the structure–activity relationships of the two scaffolds.

Synthesis of novel HDACs inhibitors

In the frame of this work, we synthesized the novel derivative NF2886, bearing a Br-substituent, and spiroindoline derivatives NF2883 and NF2889, bearing a thiophene ring as an anchor for the hydroxamate moiety (Fig. 1). Figure 2 reports the synthesis of NF2886 (panel A), NF2883 and NF2889 (panel B).

In vitro *activity of novel compounds against human and* S. mansoni *HDAC8 enzymes*

Compounds NF2886, NF2883, and NF2889 inhibit *in vitro* the enzymatic activity of *Sm*HDAC8 and *Homo sapiens* (*h*) HDAC8 recombinant proteins, the IC_{50} being in the micromolar and submicromolar range (Table 1). The previously published results for reference compounds NF2624, NF2453, and NF2452 are also reported for comparison (11).

Fluorine (NF2624) and bromine (NF2886) derivatives show similar IC_{50} toward both human and schistosoma enzymes. A major improvement in IC_{50} was detected for the spiroindoline derivatives toward *Sm*HDAC8 and hHDAC8. In particular, NF2883 shows about 20-fold enhancement in potency with respect to NF2453 toward both SmHDAC8 and hHDAC8, while NF2889 shows a 6-fold and a 2-fold improvement in potency toward parasite and human enzyme with respect to NF2452.

Novel multistage HDAC inhibitors active on schistosome larval and adult stages

The three novel molecules were tested in their ability to impair both *S. mansoni* larvae (schistosomula) and adult worm pairs viability (Fig. 3, panel *A* and *B*). The effect of inhibitors on schistosomula was assessed using an ATP-based assay previously developed and validated in our laboratory (12, 13). Compounds NF2883 and NF2889 showed to be more effective in killing parasites' larvae. Their estimated LD_{50} is similar to

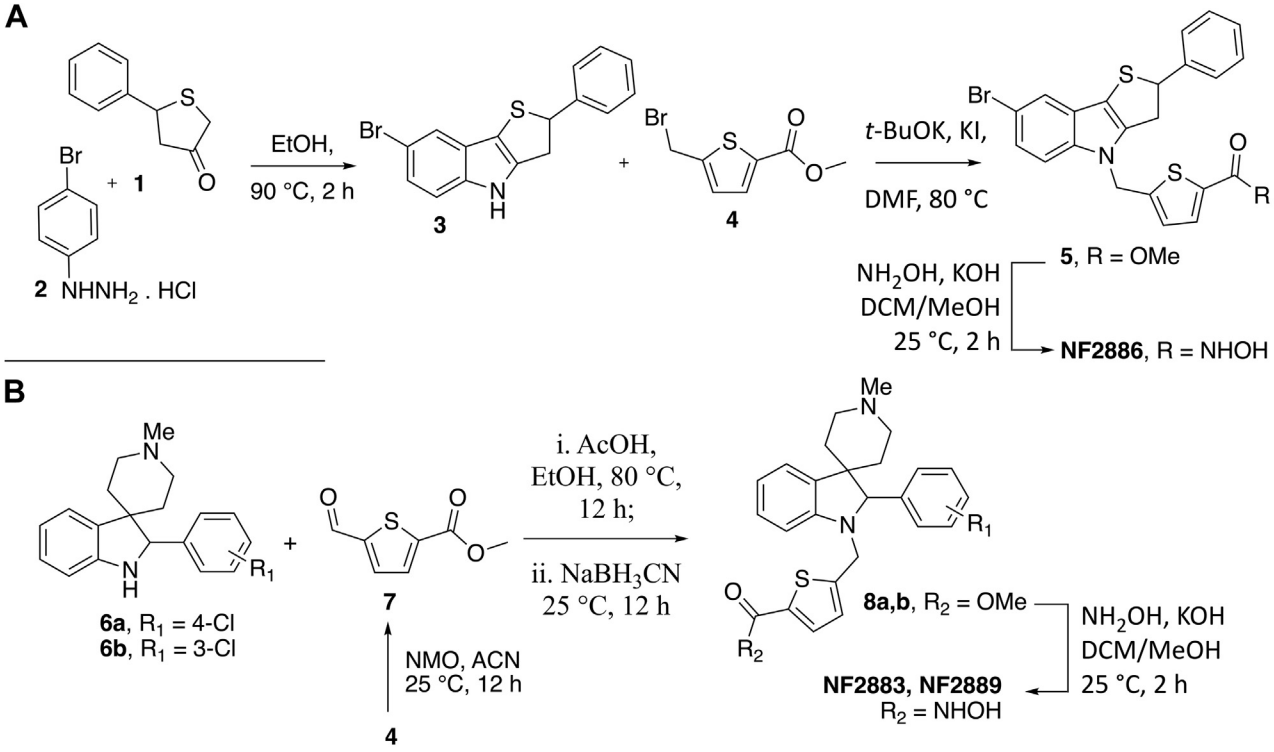

Figure 2. Synthesis of the thieno[3,2-b]indole and spiroindoline derivatives HDAC inhibitors investigated in the present work. *A*, synthesis of NF2886. *B*, synthesis of NF2883 and NF2889.

the one previously reported for NF2452 (20.59, 95% confidence interval: 11.47–24.80 μM) and NF2453 (13.31, 95% confidence interval: 11.85–15.27 μM) (11). On the contrary, NF2886 was poorly effective; the estimated LD_{50} (~60 μM) is higher than the LD_{50} of NF2624 (23.29, 95% confidence interval: 20.81–25.28 μM) previously reported (11). These results suggest that the bromine substitution has a deleterious effect on the schistosomicidal activity. Also, the impact of the three compounds on adult worm pairs viability was monitored for 7 days upon treatment. Dimethyl sulfoxide (DMSO)–treated parasites were used as negative control (100% viability) and the novel compounds were assayed at the indicated concentrations (Fig. 3*B*). Viability of each schistosome was graded from 3 (normal) to 0 (severe effect) by assigning daily worm phenotype scores as previously described (see Experimental procedures) (12, 14). The results show that NF2883 and NF2889 are slightly more potent than NF2886; in fact, at a concentration of 50 μM, both NF2883 and NF2889 caused an immediate loss of viability at 24 h. The same compounds at 20 μM markedly reduce parasite viability in a time-dependent manner, resulting in almost complete death at 7 days. Both compounds were also active at 10 μM, causing a 50% reduction of viability at day 7. On the other hand, NF2886 was less active at both 20 and 50 μM, inducing approximately a 50% reduction of viability at day 7 and being ineffective at 10 μM. In order to investigate the effects of the new compounds on HDACs activity on cultured worms, acetylation of lysine residues within histone proteins was evaluated. Based on the viability dose-responses curves, worm pairs were treated with sublethal (10 μM NF2883 72 h, 10 μM NF2886 72 h, 5 μM NF2889 72 h) or concentrations of compounds that only partially impair viability (50%) (20 μM NF2883 24 h, 20 μM NF2886 24 h, 10 μM NF2889 24 h). Next, histone-enriched fractions of parasite lysates were subjected to SDS-PAGE and Western blot analysis (Fig. 3*C*). Treatment with the pan-HDAC inhibitor Trichostatin A (TSA, 1 μM) and NF2624 (20 μM) (11) compounds were used as positive controls. About 10-fold and 7-fold increases of K-acetylation to tubulin ratio *versus* control were observed for the TSA and NF2624 treated samples. An increase of lysine acetylation signal was detected

Table 1
Estimate of IC_{50} values of HDAC8 inhibition

			Spiro-indoline derivatives			
	thieno[3,2-b]indole derivatives		*p*-chloro substituted		*m*-chloro substituted	
Class	NF2624[#]	NF2886	NF2453[#]	NF2883	NF2452[#]	NF2889
*Sm*HDAC8	1.94 ± 0.42	4.22 ± 1.58	7.71 ±2.21	0.40 ± 0.11[@]	4.36 ± 2.34	0.68 ± 0.08[@]
*h*HDAC8	2.03 ± 0.28	3.14 ± 0.57	3.45 ± 2.14	0.16 ± 0.02[#]	3.42 ± 1.28	1.32 ± 0.07[#]

The IC_{50} (μM) of the indicated inhibitors on recombinant *Sm*HDAC8 and *h*HDAC8 enzymatic activity are shown as an average of three (#) or four (@) independent experiments; uncertainties are given as SDs. (NF2886 *versus* NF2883, significance: $p < 0.005$; NF2886 *versus* NF2889, significance: $p < 0.05$; all other values between SmHDAC8 *versus* hHDAC8 are statistically significant, $p < 0.05$). The Fluor-de-Lys substrate was used at 50 μM, and the inhibitor concentrations ranged from 25 μM to 0.04 μM.

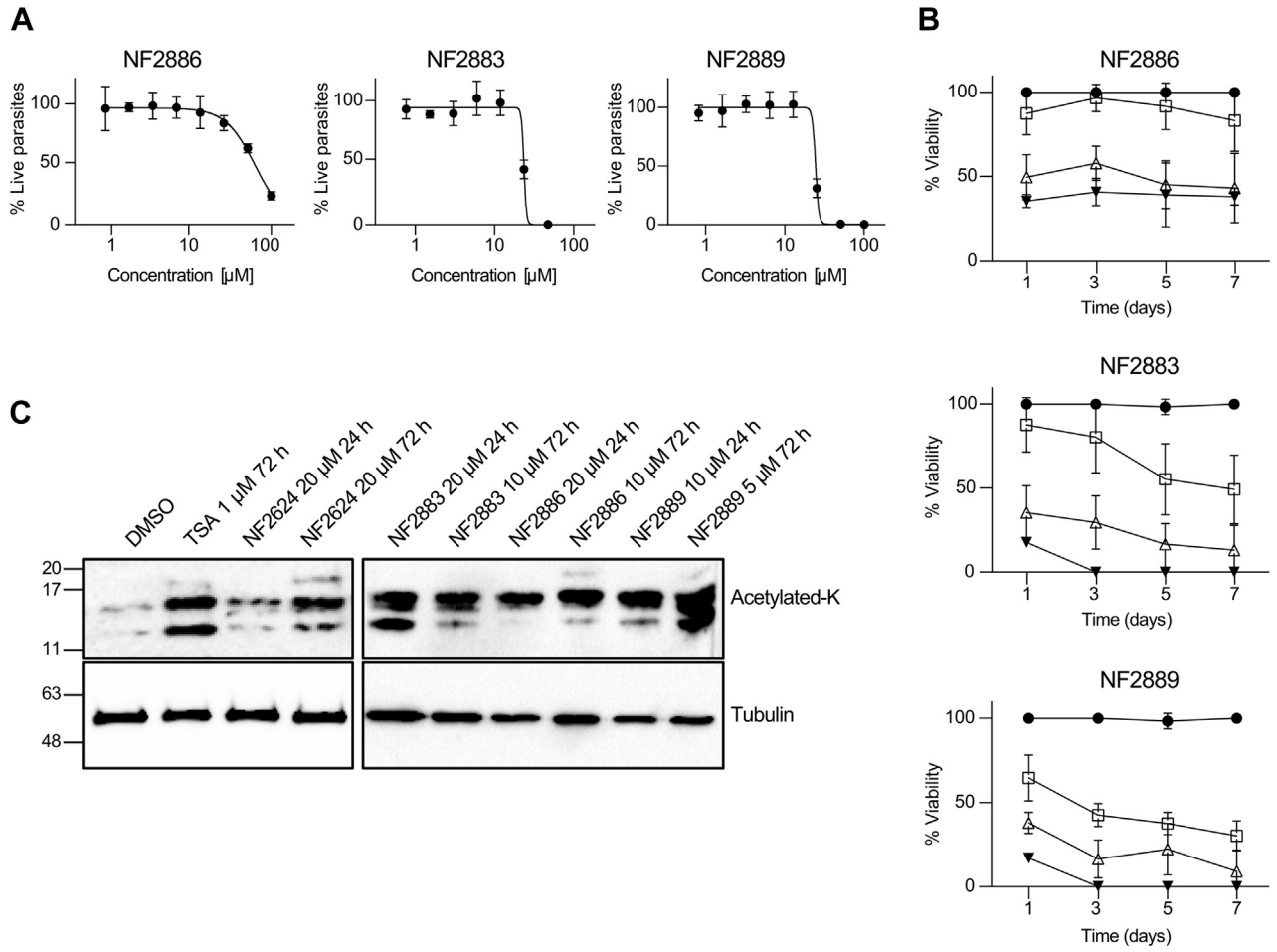

Figure 3. Viability assays and histone K-acetylation on parasites. *A*, dose-response curves of the inhibitors on schistosomula. The *y*-axis indicates the percentage of viability normalized against DMSO (100%) and gambogic acid 10 μM (0%). Each point represents the average and SD of three independent experiments. The calculated LD_{50} (μM) was as follows: NF2886, 59.9 ± 4.9; NF2883, 26.2 ± 1.1; NF2889 26.2 ± 1.6. *B*, dose-response curve of the inhibitors on adult schistosome pairs. DMSO (vehicle) was used as negative control (100% viability – *full circle*), the indicated compounds were assayed at 10 (open square), 20 (open triangle), and 50 μM (inverted full triangle). Data are expressed as a percent severity score (viability) relative to DMSO. Each point represents the average ± standard error of three independent experiments. *C*, effects of selected compounds on histones K-acetylation. Representative immunoblot of the histone-enriched protein fractions extracted from *S. mansoni* adult worm pairs incubated with antiacetylated lysine antibody (acetylated-K) or antitubulin. Worm pairs were treated for 24 or 72 h at the concentration indicated for each compound. DMSO (vehicle) and 1 μM of the HDAC pan inhibitor, TSA, were used as negative and positive controls, respectively. DMSO, dimethyl sulfoxide.

for all experimental compound-treated samples, in particular for worms treated with NF2889 at 10 μM for 24 h (6.5-fold increase *versus* DMSO) and at 5 μM for 72 h (11-fold increase *versus* DMSO) (Fig. 3*C*). Three bands ranging from ∼11 to ∼16 kDa were detected: the lower mobility bands likely correspond to the hyperacetylated forms of H2B (∼13 kDa) and H2A (∼16 kDa), whereas the one migrating faster is ascribable to histone H4 (11 kDa).

Structures of Sm*HDAC8 in complex with NF2624 and NF2886*

We obtained the crystal structures of *Sm*HDAC8 in complexes with NF2624 (Protein Data Bank [PDB] entry 7P2S) and NF2886 (PDB entry 7P2T). These structures were overall similar to previously reported structures of the enzyme bound to hydroxamate-based inhibitors in the catalytic binding site (15–20). Details about structure determination and the crystallographic data are reported in the Experimental procedures section and in Supporting Information S1. Depiction of binding and details about the binding poses for both the compounds are reported in Supporting Information S2 and S3. The full list of interactions of compounds NF2624 and NF2886 within 4 Å distance to protein residues is reported in Supporting Information S4. Moreover, we obtained a crystal structure of the enzyme with a DMSO molecule in the active site (PDB entry 7P0Z). This structure revealed that DMSO interacts with zinc and that the Tyr341 residue may adopt a flip-in conformation within the active site (Supporting Information S5). The Tyr341 conformation was previously reported in its flip-in conformation in the presence of an inhibitor bound in the active site and in its flip-out conformation in the presence of tartrate (PDB entry 4bz5; (15)). Conversely, in the structure of *Sm*HDAC8 with NF2886, in all out of the four chains, the Tyr341 was found in its flip-out conformation. These results suggest that the active site may have a number of accessible conformations of the side chains of critical residues irrespective of the molecule bound

within it. Interestingly, it is worth noting that the flip-out conformation of Tyr341 seems strictly coupled to the flip-out conformation of Phe151; indeed, the flip-out Tyr341 was found only in those structures where Phe151 is in the same conformation. The conformation of Phe151 and Tyr341 detected in all of the *Sm*HDAC8 crystal structures reported so far are listed in Supporting Information S5.

Unveiling a novel site on the surface of Sm*HDAC8: Crystal structures of* Sm*HDAC8 in complex with NF2883 and NF2889*

We also succeeded in obtaining the crystal structures of complexes of *Sm*HDAC8 with NF2883 and NF2889. Details about structure determination and crystallographic data are reported in the Experimental procedures section and in Supporting Information S1. The crystal structure of these complexes revealed that both NF2883 and NF2889 bind in a similar manner a novel site of the protein, contributed by amino acids belonging to helices α9, the loop between β5 and α9, and the loop between sheets β5 and β6. Structural superpositions of NF2883 and NF2889 are reported in Supporting Information S6. In Figure 4, the structure of SmHDAC8 in complex with NF2889 is shown. The new binding site lies on the surface of the macromolecule, ∼18 Å from the active site (taking the zinc ion as a pivot, Fig. 4*A*). The binding cleft is composed by His189, Glu194, Glu195, Trp198, Thr219, Leu234, and Asn246 residues that contribute through their main and side chains atoms, together with water molecules, to the interaction with NF2883 and NF2889 compounds. The presence of Trp198 is of outstanding importance; indeed, in the human HDAC8, the same position is occupied by a serine residue (Ser190, according to PDB entry 1t64), thus conferring a peculiar feature to this site in Schistosoma mansoni's enzyme. In addition, Glu195 in SmHDAC8 is replaced by an aspartic residue in the human ortholog (Asp187). Taking the structure of NF2889 as reference (due to its higher resolution), many characteristic interactions can be observed, with Glu195 and Trp198 showing to contribute utmost in the inhibitor binding. Indeed, the indole portion of Trp198 forms a π–π stacking with the thiophene ring along with a T-shaped hydrophobic interaction with the indoline portion of the cap group (Fig. 4B). Hydrophobic interactions are also present between the methyl-piperidine portion of NF2889 and the aliphatic carbons of Glu195. At 3.9 Å distance, Leu234 makes contact with the sulfur of the thiophene ring. On the other hand, the hydroxamate group makes hydrogen bonds with the lateral chain of Glu194 and the main chain atoms of Gly220; in addition, a water molecule bridges the hydroxamate moiety and the main chain atoms of Thr221. The full list of interactions within 4 Å distance for both NF2883 and NF2889 is reported in Supporting information S4. It is worth mentioning here that the chlorine atom is engaged by the CH_3 of Thr219 at 4.3 Å distance. This specific interaction is shared between the binding modes of both NF2883 and NF2889; however, due to the parasubstitution, NF2883 is forced to hold a slightly different position with respect to NF2889, in order to mediate the same interaction (Supporting Information S6).

Effects of perturbation by Trp198 mutation: Fluorescence spectra analysis and enzymatic activity

Trp198 is likely to have the greatest role in mediating the interactions of *Sm*HDAC8 with both NF2883 and NF2889 (Fig. 4 and Supporting Information S6). To get insights on its role and to further characterize the novel binding site, we generated a *Sm*HDAC8 W198A mutant. The comparison of the fluorescence emission of the WT *Sm*HDAC8, containing eight tryptophan residues, and the W198A was fundamental to investigate the impact of the mutation on compounds' binding. Both WT and W198A mutant proteins were incubated either with DMSO (control), NF2886, and NF2889, and fluorescence emission between 310 and 450 nm was recorded after excitation at both 280 and 298 nm wavelengths. Once incubated with NF2886 or NF2889, the fluorescence signal of WT is quenched with respect to that of control (Fig. 5, panel *A*). Similarly, the emission of the WT enzyme, recorded after

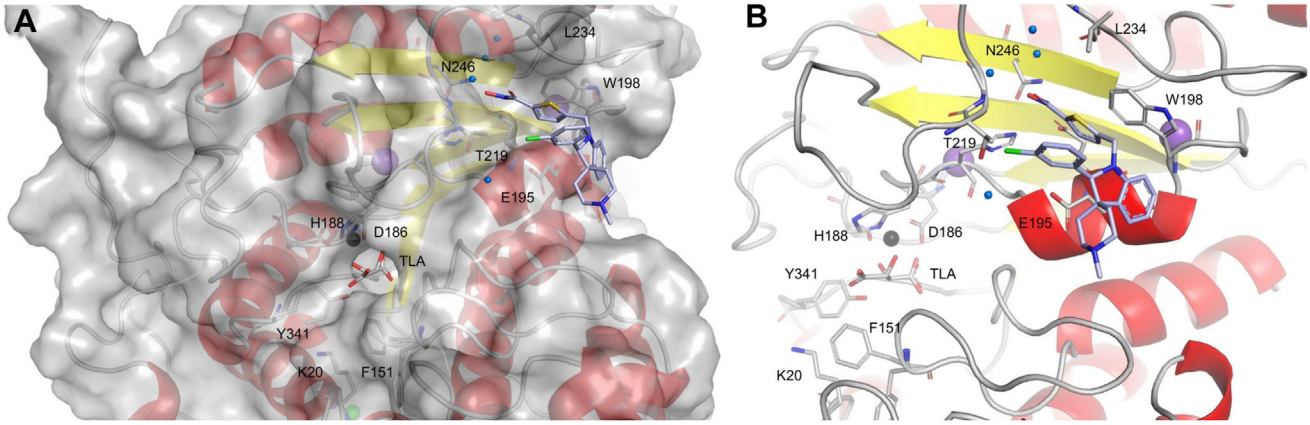

Figure 4. Cartoon representations of SmHDAC8 and NF2889 binding. *A*, binding of NF2889 on the surface of *Sm*HDAC8 on the new site; the active site is also shown. NF2889 is depicted as *light blue sticks*; loops between helices are depicted in *gray*; secondary structure elements are in *red* and *yellow*; highlighted in sticks are the side chains of the residues involved in binding interaction with NF2889. *B*, the active site is in the background where zinc ion (depicted as a *gray* sphere), TLA (standing for Na/K-tartrate), and some residues involved in catalysis are also highlighted. Water molecules involved in hydrogen bonds are represented as *blue spheres*.

excitation at 298 nm, shows a quenching of the tryptophan fluorescence with both compounds (Fig. 5*C*). On the contrary, the fluorescence spectra recorded for the W198A mutant in presence of NF2886 or NF2889 showed different spectra with respect to the ones recorded for the WT: for instance, a quenching of fluorescence after excitation at 280 nm was observed only in presence of NF2886 but not with NF2889 (Fig. 5*B*). In addition, after excitation at 298 nm, the signal of the mutant incubated with NF2886 still shows a quenching; on the other hand, incubation with NF2889 shows a spectrum similar to the one of the control sample (Fig. 5*D*). Additional experiments were performed with 2 mM Na/K-tartrate, in order to mimic the conditions used in the crystallization trials. Interestingly, the strongest influence of tartrate was detected with the *Sm*HDAC8 mutant incubated with NF2886. In this case, the fluorescence signal, recorded after excitation at 298 nm, was less quenched and showed a shape of the spectrum (Supporting Information S7, panel G), different to the one without tartrate (Supporting Information S7, panel *D*). This behavior can likely be ascribed to the relative competition by tartrate and NF2886 in their binding to the active site. The fluorescence spectra of WT and mutant incubated with NF2889 were not perturbed by the presence of tartrate, as expected for the binding to a different site (Supporting Information S7). Remarkably, the mutation W198A had also a strong impact on the enzymatic activity of *Sm*HDAC8: indeed, the W198A mutant shows only about 40% of residual activity with respect to the WT enzyme in the same experimental conditions (Table 2).

This finding, along with the inhibition studies reported below on the WT *Sm*HDAC8, raises the suspicion of an allosteric inhibition by NF2889 upon binding to the novel site. Indeed, perturbing the region either by a point mutation or by inhibitor binding results in a decrease in the enzymatic activity.

On the nature of NF2886 and NF2889 as SmHDAC8 inhibitors

The structural data and fluorescence studies on SmHDAC8 suggest the possibility that the molecules NF2624/NF2886 and NF2883/NF2889 are acting by a different mechanism of inhibition. Both NF2624 and NF2886, which bind the enzyme active site, allegedly would behave as competitive inhibitors;

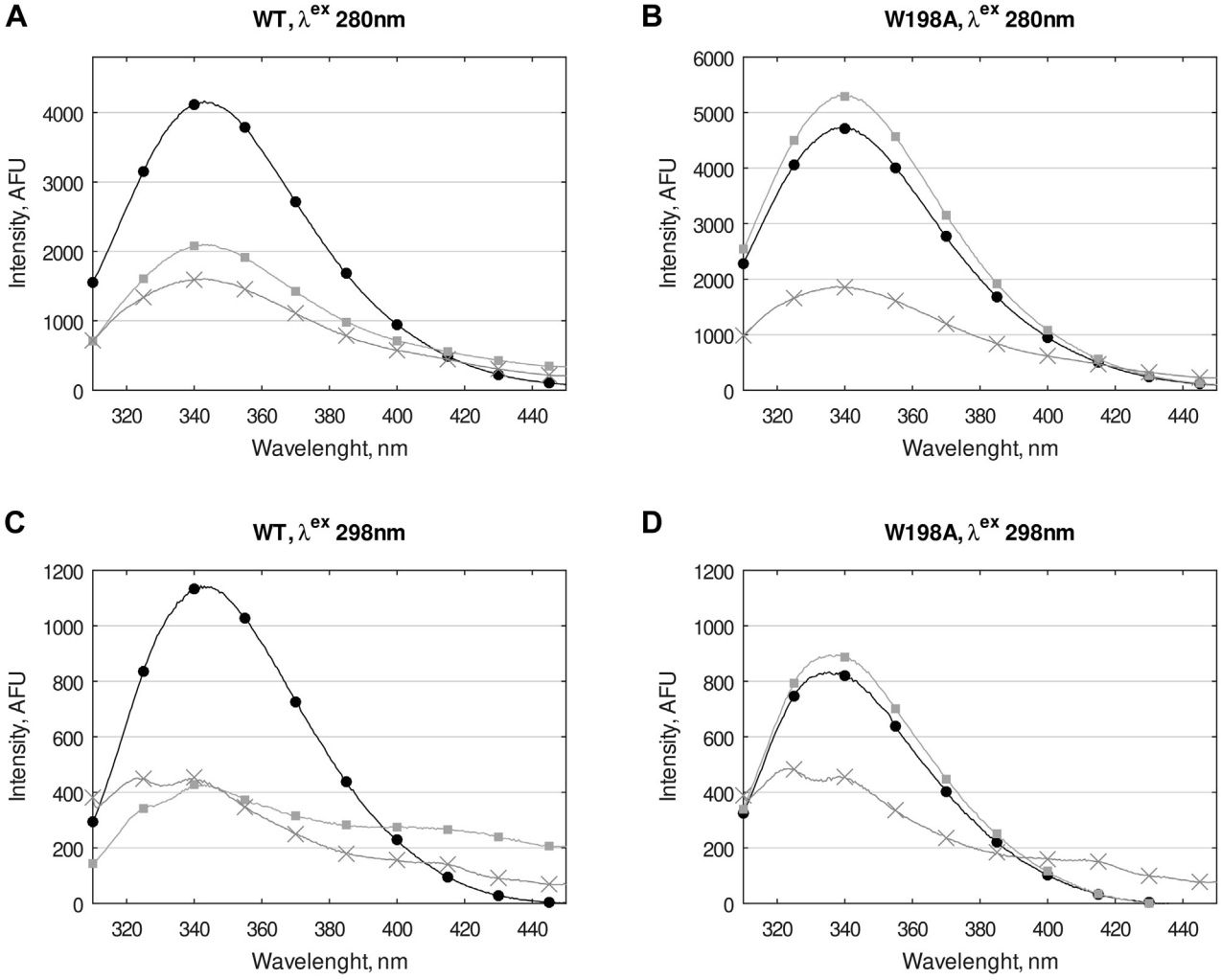

Figure 5. Fluorescence emission spectra of *Sm*HDAC8 in complexes with NF2886 and NF2889. *A*, WT, excitation 280 nm; *B*, W198A mutant, excitation 280 nm; *C*, WT, excitation 298 nm; *D*, W198A, excitation 298 nm. NF2886 (*gray* cross marker) and NF2889 (*gray* squares). DMSO is included for comparison, as control (*full circles*).

Table 2
Comparison of the enzymatic activities of the W198A mutant and WT *Sm*HDAC8 proteins

	WT*	W198A#
Activity, %	100	37.8 ± 8.1

Average of three (*) or five (#) independent experiments ± SD (statistical significance, $p < 0.01$. Protein concentration was 0.6 μM and substrate concentration was 50 μM.

Table 4
Calculated K_i (μM) for the binding to *Sm*HDAC8

	NF2886*	NF2883*	NF2889#
K_i	9.7 ± 7.2	0.13 ± 0.05	0.6 ± 0.2

Average of three (*), or four (#) independent experiments ± SD. (statistical significance of NF2883 and NF2889 vs NF2886, $p < 0.05$).

conversely, the inhibition by NF2883/NF2889 was expected to show a different feature due to binding to the novel site. To investigate the type of inhibition, steady-state kinetic experiments on *Sm*HDAC8 and *h*HDAC8 were performed, with a fixed concentration of either NF2886 or NF2889 (taken as representative for alleged competitive and for a mixed mechanism of inhibition, respectively). The results are reported in Table 3.

Inhibitor concentrations were chosen on the basis of the IC_{50} (Table 1; see Experimental procedures). Table 3 highlights differences in the steady-state parameters of *Sm*HDAC8 incubated with vehicle or with 5 μM NF2886. With the inhibitor, it was observed more than a 3-fold increment of K_M, whereas the k_{cat} was unaffected; these data identified this molecule as a competitive inhibitor in agreement with the structural finding of NF2886 bound to the active site. On the contrary, the kinetics data obtained for *Sm*HDAC8 incubated with 1 μM NF2889 reveal a more complex profile, since both k_{cat} and K_M decreased. Interestingly, in this case, the ratio k_{cat}/K_M is slightly higher than control (Table 3). This in turn suggests the presence of a mixed-type inhibition (21), with a substrate-enhancement effect (22), although the large experimental error associated with k_{cat} and K_M makes it difficult to assign the inhibition profile with a high degree of confidence. Surprisingly, *h*HDAC8 showed to be inhibited by both NF2886 and NF2889 in the same competitive way (Table 3), being K_M increased and k_{cat} unaffected. Next, the binding affinity of NF2883, NF2886, and NF2889 to *Sm*HDAC8, in absence of substrate, was obtained by monitoring the quenching of the intrinsic fluorescence of the enzyme after its incubation with increasing concentrations of the compounds (see Experimental Procedures); the obtained K_i, defined as dissociation constant, are reported in Table 4.

Interestingly, the K_i values show that the intrinsic affinities of NF2889 and NF2883 for *Sm*HDAC8 are greater than the affinity of NF2886 in agreement with the estimated IC_{50} of the compounds (Table 1). Moreover, the steady-state kinetics (increased k_{cat}/K_M ratio) and binding data show that the binding of NF2889 and substrate to *Sm*HDAC8 influence each other suggesting an allosteric mechanism of inhibition. To assess the putative substrate-enhancement effect over NF2883 and NF2889 potency, IC_{50} estimate were assessed at different concentrations of substrate (50 and 150 μM Fluor-de-Lys). In the same experimental conditions, IC_{50} was also estimated for NF2886 (Table 5).

The IC_{50} for NF2886 shows about a 2-fold increase with 150 μM concentration of substrate, thus confirming the competitive nature of inhibition for this compound. On the contrary, the IC_{50} for NF2883 and NF2889 shows a decrease (hence, a better potency) with an increased concentration of substrate. This finding confirmed that the inhibitor's potency is substrate dependent and confirmed a mixed-type inhibition with a substrate-enhanced effect for NF2883 and NF2889 toward *Sm*HDAC8.

Phylogenetic studies on parasites' HDAC8

To explore the conservation and evolution of the *Sm*HDAC8 novel site, we inferred the phylogenetic tree based on the protein sequences of *Sm*HDAC8 orthologs from parasites belonging to different phyla. The maximum-likelihood inferred tree is depicted in Figure 6 (panel *A*). All the extant Platyhelminthes' HDAC8 clusters are in the same clade. A deeper analysis of the multiple sequence alignment revealed that the couple of residues corresponding to Trp198 and Leu234 in *Sm*HDAC8 sequence is conserved among all the *Schistosoma* spp and in all Platyhelminthes belonging to both Rhabidoptera and Trematoda classes (Fig. 6, panel *B*). Interestingly, *Schistosoma* genus has a TWNM-X-DNDKLP motif, which is about 30 amino acids apart from W198, a region corresponding to the loop between β5 and β6 in the *Sm*HDAC8 structure. This loop and the residues therein are in close contact with some residues of the active site, suggesting that structural information can be propagated throughout upon perturbation on the novel site. *Sm*HDAC8 W198A and compound binding experiment results support this hypothesis. A similar loop is recognizable in the sequence alignment of other species within the same group, namely *Opisthorchis felineus*, *Opistrochis viverrini*, *Clonorchis sinensis*, and *Paragonimus westermani*. The complete amino acid sequence

Table 3
Steady-state kinetics parameters for *Sm*HDAC8 WT and *h*HDAC8

Enzyme	*Sm*HDAC8			*h*HDAC8[§]		
Conditions	Ctrl (DMSO)*	5μM NF2886#	1μM NF2889*	Ctrl (DMSO)	5μM NF2886	2μM NF2889
k_{cat} (s^{-1})	0.017 ± 0.004	0.017 ± 0.003	0.007 ± 0.003	0.010 ± 0.001	0.012 ± 0.004	0.011 ± 0.005
K_M (μM)	737 ± 197	2403 ± 1590	273 ± 163	302 ± 4.5	1119.5 ± 70.5	662.5 ± 53.5
k_{cat}/K_M	22.8	7.2	25.6	31.4	10.7	15.8

Average of four (*), three (#), or two ([§]) independent experiments ± SD (for SmHDAC8, statistical significance of NF2889 *versus* Ctrl, $p < 0.05$).

Table 5
Calculated IC_{50} (μM) for the inhibitors at different substrate concentrations

	NF2886		NF2883		NF2889	
Substrate, μM	50	150	50	150	50	150
IC_{50}	5.17 ± 2.58	9.56 ± 3.29	0.110 ± 0.011	0.041 ± 0.002	0.37 ± 0.13	0.055 ± 0.007

Average of two independent experiments ± SD. (50 μM *vs* 150 μM comparison: statistical significance, $p < 0.05$).

alignment, generated by PRANK, is reported in Supporting Information S9. Noteworthy, in *h*HDAC8 and many other vertebrates, W198 is replaced by a serine residue (Supporting Information S10).

The conservation of the novel *Sm*HDAC8 site in Platyhelminthes may be important for the development of new drugs: it is likely that a compound binding in this region can interfere with the activity of HDAC8 within members of the same clade.

Discussion

*Sm*HDAC8 emerged as a good target for the development of new synthetic compounds with schistosomicidal activity (23, 24). Several compounds have been shown to inhibit the enzymatic activity of recombinant *Sm*HDAC8 in the nanomolar to mid-micromolar range by binding the active site (10, 11, 15–20). So far, the identified compounds are likely acting as competitive inhibitors, although in the majority of studies, the actual nature of the enzyme inhibition was not deeply investigated. Su *et al.* timely proposed noncompetitive inhibitors as a not yet exploited path to get more selective compounds and to avoid off-target activity against different HDAC isoforms or other zinc-containing proteins (25). Indeed, the hydroxamic-based inhibitors pose a great challenge from a pharmacological point of view due to the zinc chelating properties. By binding to a unique allosteric site, rather than at the catalytic active site, compounds acquire higher selectivity toward enzymes utilizing the same substrate or reaction mechanism (26). Incubation of *Sm*HDAC8 with NF2883 or NF2889 resulted in an inhibition of *Sm*HDAC8 activity *in vitro* and in antischistosomal activity on both larvae and adult parasite stages. Steady-state kinetics experiments demonstrated that NF2889 behaves as a mixed/allosteric inhibitor, being both k_{cat} and K_M lowered with respect to a competitive inhibitor such as NF2886 (Table 3). The findings along with the fluorescence-binding experiments (Table 4) suggest that the equilibrium between the enzyme, the substrate, and NF2889 follows the scheme, according to Bellelli and Carey, reported below for mixed-type inhibitors (27):

$$\begin{array}{ccc} E + S & \overset{K_M}{\rightleftarrows} & ES \rightarrow E+P \\ + & & + \\ I & & I \\ \uparrow\downarrow K_i & & \uparrow\downarrow {}^{s}K_i \\ EI + S & \underset{{}^{i}K_M}{\rightleftarrows} & ESI \end{array}$$

The ${}^{s}K_i$, the affinity constant of the inhibitor in presence of substrate, results to be equal to 0.21 μM, as obtained from the ratio $({}^{i}K_M \cdot K_i)/K_M$ for NF2889 (Tables 3 and 4) or 0.06 μM from the Cheng–Prusoff equation for mixed inhibitors (28), obtained from IC_{50}s data (Table 5). This confirmed that the inhibitor ranks among the mixed-type inhibitors, whose affinity is enhanced by the substrate binding, being its $K_i > {}^{s}K_i$ (21, 22, 27).

Crystal structures demonstrated how NF2883 and NF2889 bind a new region of the surface of *Sm*HDAC8, not previously exploited. Both competitive and mixed-type/allosteric compounds quenched the fluorescence emission signal of the WT enzyme, whereas only NF2886 binding to the active site had an impact on the mutant form. In addition, the fluorescence spectra suggest that NF2889 can bind only to the novel site and not to the catalytic site since no quenching was detected with the SmHDAC8 mutant at all. Overall, structural and functional data point out the possibility of an allosteric structural transition accompanying the binding of inhibitors NF2883 and NF2889.

Allosteric regions have been recently described in *h*HDAC8, the so-called 'binding-rail' and loop 2 (further spread into 2A and 2B) (29) and a distal helix1-loop1-helix2 regulatory region (9). It has been proposed that the *h*HDAC8 enzyme populates alternative inactive and active states (9). A bidirectional, regulatory communication between a distal helix1-loop1-helix2 region and the active site of HDAC8 was demonstrated (9). Indeed, changes in the active site, by TSA binding, cause perturbation of residues in the distal region while perturbations of residues in the helix1-loop1-helix2 regulatory region, by mutations, affected residues near the active site (9). Recently, loops 1 to 7, which contribute to active site fold in *h*HDAC8, were sampled by molecular dynamics simulation on 10 μm time scale, revealing that some slight movements of aromatic side chains (namely F152 and Y306) within active site take place upon substrate or inhibitors' binding and translate into the opening or closing of the active site (30). Overall, these studies point out the nature of intrinsic flexibility of loops surrounding the *h*HDAC8 active site as a major contribution to enzyme activity and regulation. Here, we demonstrate a mixed-type/allosteric inhibition of *Sm*HDAC8 upon binding of spiroindoline-harboring compound in a new regulatory site, contributed by residues W198, E195, T219, L234, and the residues in the nearby, as revealed by crystal structures 7P2U and 7P2V. The 'binding rail', which is contributed by Y100 and D101 in *h*HDAC8, is conserved in *Sm*HDAC8, aligning to positions 99 and 100, respectively. Loop 2—contributed by residues spanning 80 to 85 (loop 2A) and 96 to 106 (loop 2B) in *Sm*HDAC8—is conserved as well. Interestingly, the best structural superposition of our *Sm*HDAC8 structures reveals small differences in loop 2 and in the 'binding rail' conformation (Fig. 7, bottom left). Such differences are likely due to binding of molecules either to the catalytic or to the novel

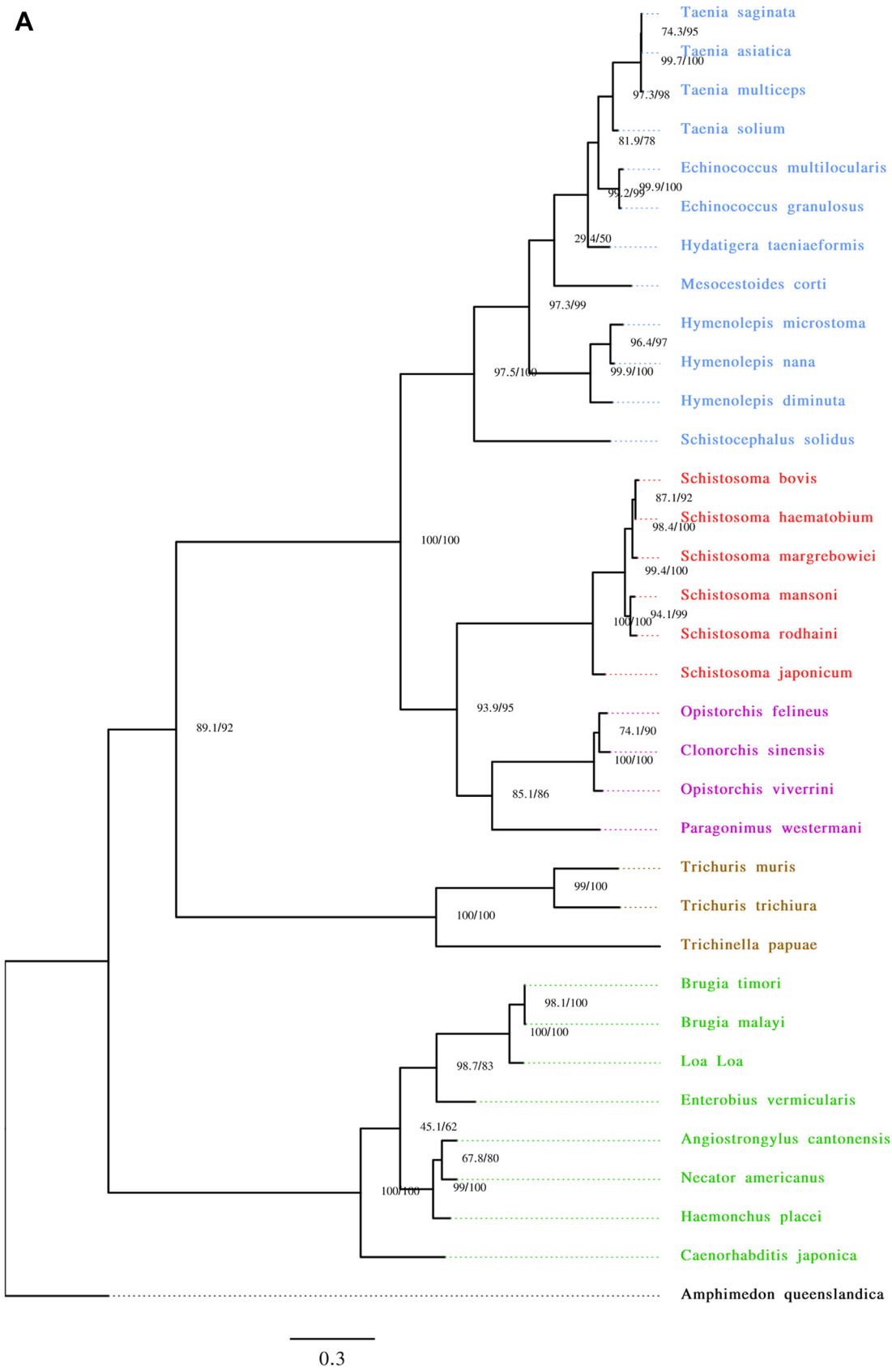

Figure 6. HDAC8 phylogenetic tree and conservation of the novel site. *A*, maximum-likelihood phylogenetic tree inference of orthologs of *Sm*HDAC8 based on sequences retrieved from WormBase ParaSite (entry WBGT00950000411223) and Ensembl Metazoa (see Experimental procedures). Details on protein sequences used are given in Supporting Information S8. Sequences belonging to the Schistosoma genus are labeled in *red*; Rhabditophora class and

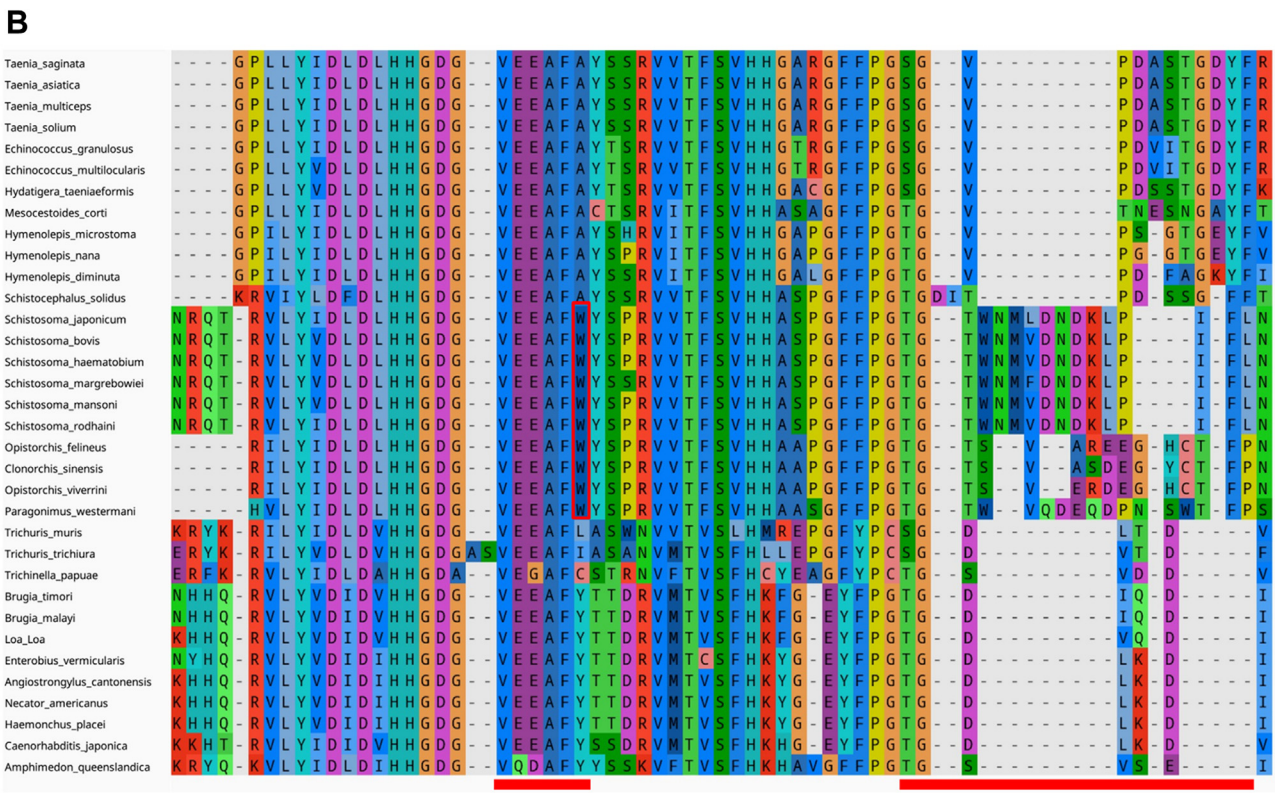

Figure 6. continued

*Sm*HDAC8 site. We observed differences in the placement of all the loops surrounding the active site, namely the loop 1, loop 2, loop β5-β6, loop β7-α11, and loop β8-α12 in all inhibitors' complexes, either the ones bound to the active site or the ones bound to the novel site. Misalignment of several loops was observed in all structures: the most dramatic variation is observed in the folding of the loop β5-β6 against the protein core in the case of NF2624/NF2886 (chain A to C) and NF2883/NF2889 (Fig. 7, bottom left). To quantify the structural variations observed, we calculated the sum of distances of the Cα of key residues with respect to zinc and noticed that, on average, they are greater in inhibitors' complexes than in DMSO-bound structure (Supporting Information S11, all distances indicated are in Å). Noteworthy, the largest movements in Cα positions (according to the calculated mean of distances of any Cα with respect to DMSO) are detected for His292 (loop β7-α11), Tyr341 (loop β8-α12), Lys20 (loop 1), Tyr99, and Asp100 (loop 2) (Supporting Information S11 highlights the four largest deviations). To further support these findings, we performed a principal component (PC) analysis (PCA). PCA has been proved to detect conformational differences in protein structures, which ultimately correlate to functional activities (31). PCA was recently applied to get insights into the conformational ensembles and space sampling of GroEL (32), heterotrimeric G proteins (33), and *Xanthomonas citri* phosphohexomutase structures (34). Hence, PCA was performed on the best-fit structural alignment of all our structures; as a result, the first three PCs accounted for 98% of the total variance (Fig. 7). Highlighted are also trajectories that have been produced by interpolating between the most dissimilar structures distributed along the first three PCs. The analysis shows that the different conformation of loops, surrounding the active site, accounted for a large portion of the detected structural variations, best represented in PC2 and PC3 (Fig. 7 and Supporting Information S12). However, loops β7-α11 and α13-α14, which are not in close contact with the active site, contribute to the largest separation detected in PC1 (Fig. 7 and Supporting Information S12).

Taken together, these findings foster the idea that, upon inhibitors' binding to the novel site, an allosteric transition could be mediated by small movements of the loops surrounding the active site, which ultimately translates into a modulation of the enzymatic activity.

In conclusion, the data revealed a novel binding site on the surface of *Sm*HDAC8. By perturbing this site, either by mutation of the Trp198 or by compound binding, a decrease in the enzyme activity is achieved. Two novel compounds, NF2883 and NF2889, bind the new site and likely inhibit the enzyme in a mixed-type/allosteric fashion. The novel site

other Trematodes are in *purple*; Cestoda are in *blue*; Nematoda are in *green*, with Enoplea class in *brown*. *Amphimedon queenslandica* (Porifera) sequence was inserted as an outgroup and used to root the tree (*bottom*, *black*). Nodes report the confidence obtained by both fast SH-aLRT and ultrafast bootstrap with 5000 replicates each. *B*, the region of the multiple sequence alignment corresponding to the novel site in *Sm*HDAC8 (entry Smp_091990) is highlighted with *red line* alongside with residues contributing to the loop β5-β6; the position corresponding to W198 in *Sm*HDAC8 is *boxed in red*.

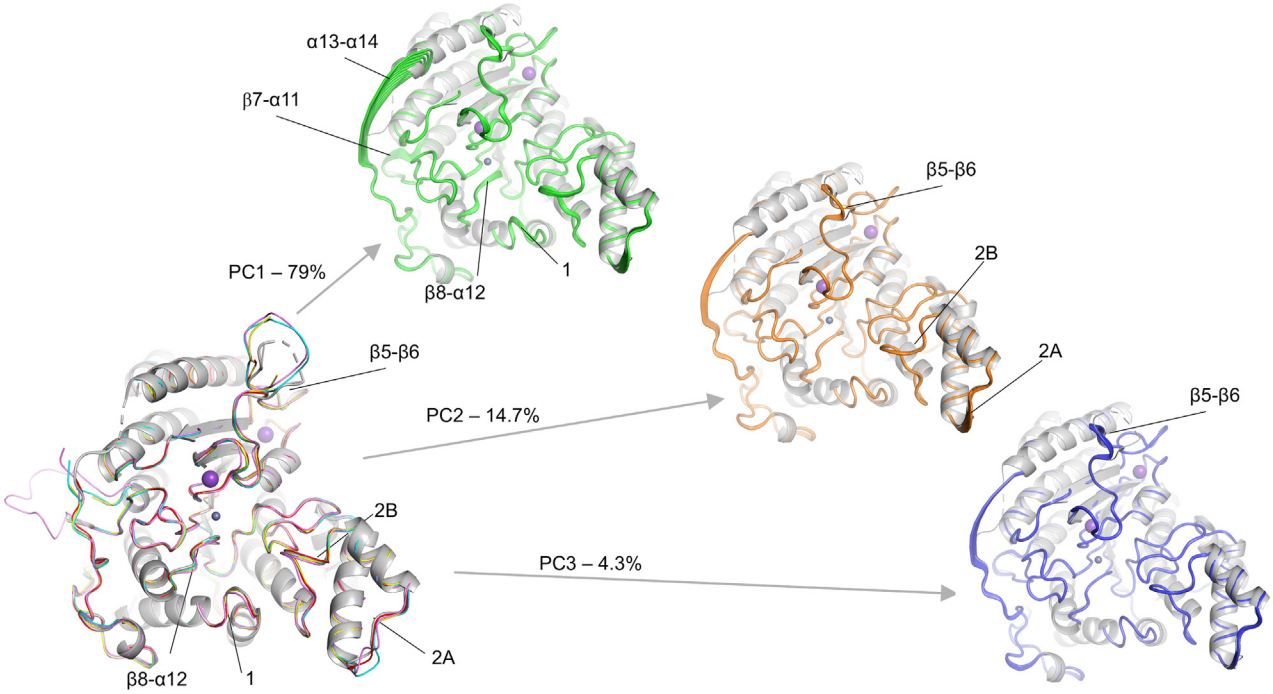

Figure 7. Structural superposition of DMSO-bound (*gray* cartoon), NF2624 (*red* ribbon), NF2886 (*purple* ribbon), NF2883 (*yellow* ribbon), and NF2889 (*cyan* ribbon) complexes (*bottom-left*). Metals are depicted as spheres: zinc, in *gray*, potassium, in *violet*. Inhibitors were omitted for clarity. The figure highlights how the folding of loops surrounding the active site are affected by inhibitors binding; in particular, the binding of NF2889 determines the largest variation in the position of loop 2A/B (residues 80–85 and 97–106, respectively) and loop β5-β6 (residues 210–243). Interestingly, any mobile loop contains some of the key residues, which are directly or indirectly involved in catalysis, in particular loop 1 (residues 16–24) contains K20; loop 2 which contributes with binding rail couple, Y99 and D100; loop β8-α12 (residues 337–342), β7-α11 (residues 281–317), and loop β5-β6 (residues 210–243) contain all the key residues involved in catalysis, D186, H188, D286, and Y341. Best-fit structural superposition was achieved by the Bio3d package within R software (35). Side panels report the trajectories of interpolated structures obtained after PCA for the first three PCs. The largest variations are highlighted and labeled according to loop numbering as reported in Marek *et al.*, 2013 (15). DMSO, dimethyl sulfoxide; PCA, principal component analysis.

diverges between *Schistosoma* and the human ortholog, both in amino acid composition and structural features. These findings pave the way to the development of a new class of selective molecules for *Sm*HDAC8. Multiple sequence alignment of parasites' HDAC8 orthologs coupled to phylogenetic studies revealed that amino acid sequence features of the enzyme are shared among *Schistosoma* spp and others Platyhelminthes.

Experimental procedures

Chemistry

All chemicals and reagents were purchased from commercial sources and used without any further purification, unless and otherwise specified. Reaction progress was monitored by TLC, carried out on silica (60 F254) or alumina (60 F254, basic) gel plates with detection by UV, and the products were purified by using either silica (60 M, 0.040–0.063 μm) or alumina (90, standardized) column chromatography. ^{1}H and ^{13}C NMR spectra were recorded in the indicated deuterated solvent on a Varian 300 MHz spectrometer by using the residual signal of the deuterated solvent as internal standard. Splitting patterns are indicated by s (singlet), d (doublet), dd (doublet of doublets), t (triplet), q (quartet), m (multiplet), and br (broad); chemical shifts (δ) are described in ppm and coupling constants (J) in Hertz (Hz). Electrospray ionization-mass spectrometry (ESI-MS) spectra were performed by an Agilent 1100 Series LC/MSD spectrometer. Yields refer to purified products and are not optimized. All moisture-sensitive reactions were performed under nitrogen atmosphere using oven-dried glassware and freshly distilled anhydrous solvents. Compounds **1**, **4**, and **6a,b** were reported in Figure 2 were prepared as previously described (11)

7-Bromo-2-phenyl-3,4-dihydro-2H-thieno[3,2-b]indole (3)

To a solution of 5-phenyldihydrothiophen-3(2H)-one (**1**, 70 mg, 0.39 mmol) in EtOH (2.5 ml), 4-bromophenylhydrazine hydrochloride (**2**, 113 mg, eq., 0.51 mmol) was added and the mixture was stirred at 90 °C for 2 h. Heating was removed and the solvent was evaporated under reduced pressure. The crude residue was purified by silica gel column chromatography (Pet. Et./AcOEt 4:1) to afford the title compound as a brown solid (88.0 mg, 69% yield). ^{1}H NMR (300 MHz, $CDCl_3$) δ 8.03 (br, 1H), 7.49 to 7.38 (m, 3H), 7.36 to 7.24 (m, 2H), 7.14 to 6.98 (m, 1H), 6.72 (t, J = 7.4 Hz, 1H), 6.53 (d, J = 7.8 Hz, 1H), 5.51 (t, J = 8.5 Hz, 1H), 3.50 (dd, J = 15.4, 8.5 Hz, 1H), and 3.36 (dd, J = 15.4, 8.4 Hz, 1H). ESI-MS m/z $[M + H]^+$ 330, 332 (1:1 ratio).

Methyl 5-((7-bromo-2-phenyl-2,3-dihydro-4H-thieno[3,2-b]indol-4-yl)methyl)thiophene-2-carboxylate (5)

To a solution of 7-bromo-2-phenyl-3,4-dihydro-2H-thieno [3,2-b]indole (**3**, 100 mg, 0.30 mmol) in anhydrous dimethylformamide (3 ml), t-BuOK (46.0 mg, 0.45 mmol), methyl 5-(bromomethyl)thiophene-2-carboxylate (**4**, 105 mg,

0.41 mmol), and KI (5 mg, 0.03 mmol) were subsequently added. The mixture was heated to 80 °C and stirred for 2 h, then heating was removed, and the mixture was stirred at 25 °C for 12 h. Reaction was quenched with NH_4Cl (s.s., 10 ml) and extracted with AcOEt (3 × 5 ml). The combined organic phases were washed with $NaHCO_3$ (s.s., 5 ml) and brine (5 ml), dried over Na_2SO_4, and evaporated under reduced pressure. The crude residue was purified by Al_2O_3 gel column chromatography (Pet. Et./AcOEt 4:1) to afford the title compound as a brown solid (61 mg, 42% yield). ^{1}H NMR (300 MHz, $CDCl_3$) δ 7.60 (d, J = 3.8 Hz, 1H), 7.53 (s, 1H), 7.44 (m, 2H), 7.36 to 7.20 (m, 4H), 7.15 (m, 1H), 6.82 (d, J = 3.7 Hz, 1H), 5.52 (t, J = 8.3 Hz, 1H), 5.35 (s, 2H), 3.91 (s, 3H), 3.55 (dd, J = 15.6, 8.5 Hz, 1H), and 3.34 (dd, J = 15.6, 8.2 Hz, 1H). ESI-MS *m/z* $[M + H]^+$ 484, 486 (1:1 ratio).

5-((7-Bromo-2-phenyl-2,3-dihydro-4H-thieno[3,2-b]indol-4-yl) methyl)-N-hydroxythiophene-2-carboxamide (NF2886)

To a solution **5** (61.0 mg, 0.13 mmol) in DCM (2 ml) and methanol (6 ml), NH_2OH (50 wt. % in H_2O, 0.83 ml, 12.6 mmol) was added, followed by a dropwise addition of methanolic KOH (4 M, 1.57 ml, 6.3 mmol) solution, and the mixture was stirred at 25 °C for 2 h. The reaction was quenched by slow addition of 1 N HCl until pH = 7. The solvent was removed under reduced pressure and the crude residue was purified by silica gel column chromatography (DCM/MeOH/NH_4OH 12:1:0.1) to afford the title compound as a yellow solid (22 mg, 35% yield). ^{1}H NMR (300 MHz, MeOD) δ 7.49 to 7.41 (m, 2H), 7.37 (m, 5H), 7.33 to 7.18 (m, 2H), 6.95 (d, J = 3.3 Hz, 1H), 4.99 to 4.77 (m, 3H), 3.61 (dd, J = 15.8, 8.4 Hz, 1H), and 3.35 (dd, J = 15.7, 8.4 Hz, 1H). ^{13}C NMR (75 MHz, MeOD) δ 161.01, 141.87, 138.77, 138.60, 128.69, 128.22 (2C), 127.95, 127.40, 126.86 (2C), 125.91, 124.38, 123.49, 120.44, 112.62, 111.64, 110.85, 58.44, 43.16, and 35.72. ESI-MS *m/z* $[M+Na]^+$ 507, 509 (1:1 ratio).

Methyl 5-formylthiophene-2-carboxylate (7)

A round bottom flask equipped with 4 Å molecular sieves under nitrogen atmosphere was charged with a solution of *N*-methylmorpholine-*N*-oxide (193 mg, 1.65 mmol) in acetonitrile (1.5 ml). The flask was cooled to 0 °C and a solution of **4** (212 mg, 0.55 mmol) in acetonitrile (2.5 ml) was added. The ice bath was removed, and the reaction mixture was stirred at 25 °C for 12 h. Then, the crude was filtered and the solvent was evaporated. The crude was purified by silica gel column chromatography (Pet. Et./AcOEt 10:1) to afford the title compound as an off-white solid (59.8 mg, 64% yield). ^{1}H NMR (300 MHz, $CDCl_3$) δ 9.97 (s, 1H), 7.84 (d, J = 3.9 Hz, 1H), and 7.73 (d, J = 4.0 Hz, 1H), 3.94 (s, 3H). ESI-MS *m/z* $[M+Na]^+$ 193.

Methyl 5-((2-(4-chlorophenyl)-1′-methylspiro[indoline-3,4′-piperidin]-1-yl)methyl)thiophene-2-carboxylate (8a)

To a solution of **6a (**46.0 mg, 0.147 mmol) in EtOH (2.3 ml), methyl 5-formylthiophene-2-carboxylate (**7,** 30.1 mg, 0.176 mmol) and acetic acid (100 µl, 0.02 mmol) were subsequently added. The reaction mixture was heated to 80 °C and stirred for 12 h. Then, the heating was removed, $NaBH_3CN$ (2 eq., 2 mmol) was added, and the mixture was stirred at 25 °C for additional 12 h. Reaction was quenched with $NaHCO_3$ (s.s., 10 ml) and extracted with AcOEt (3 × 10 ml). The combined organic phases were washed with brine (15 ml), dried over Na_2SO_4, and evaporated under reduced pressure. The crude residue was purified by silica gel column chromatography (DCM/MeOH 10:1) to afford the title compound as a yellow oil (32 mg, 47% yield). ^{1}H NMR (300 MHz, $CDCl_3$) δ 7.63 (d, J = 3.7 Hz, 1H), 7.38 to 7.20 (m, 4H), 7.20 to 7.06 (m, 2H), 6.87 to 6.73 (m, 2H), 6.53 (d, J = 7.8 Hz, 1H), 4.47 (d, J = 16.2 Hz, 1H), 4.36 (s, 1H), 4.04 (d, J = 16.2 Hz, 1H), 3.85 (s, 3H), 2.98 to 2.81 (m, 1H), 2.77 to 2.64 (m, 1H), 2.63 to 2.49 (m, 1H), 2.38 (s, 3H), 2.25 to 1.76 (m, 4H), and 1.59 to 1.37 (m, 1H). ESI-MS *m/z* $[M + H]^+$ 467, 469 (3:1 ratio).

Methyl 5-((2-(3-chlorophenyl)-1′-methylspiro[indoline-3,4′-piperidin]-1-yl)methyl)thiophene-2-carboxylate (8b)

Following the same procedure described for compound **8a**, the title compound was obtained starting from 2-(3-chlorophenyl)-1′-methylspiro[indoline-3,4′-piperidine] (**6b**) and methyl 5-formylthiophene-2-carboxylate (**7**), after purification by silica gel column chromatography (DCM/MeOH 30:1) as a yellow oil (57 mg, 40% yield). ^{1}H NMR (300 MHz, $CDCl_3$) δ 7.63 (s, 1H), 7.39 to 7.00 (m, 6H), 6.79 (m, 2H), 6.63 to 6.38 (m, 1H), 4.58 to 4.26 (m, 2H), 4.06 (d, J = 16.3 Hz, 1H), 3.85 (s, 3H), 2.91 to 2.75 (m, 1H), 2.75 to 2.43 (m, 2H), 2.34 (s, 3H), 2.25 to 1.75 (m, 4H), and 1.57 to 1.35 (m, 1H). ESI-MS *m/z* $[M + H]^+$ 467, 469 (3:1 ratio).

5-((2-(4-chlorophenyl)-1′-methylspiro[indoline-3,4′-piperidin]-1-yl) methyl)-N-hydroxythiophene-2-carboxamide (NF2883)

Following the same procedure described for compound NF2886, the title compound NF2883 was obtained starting from **8a**, after purification by silica gel column chromatography (DCM/MeOH/NH_4OH 10:1:0.1) as an off-white solid (45 mg, 40% yield). ^{1}H NMR (300 MHz, MeOD) δ 7.50 to 7.17 (m, 6H), 7.10 (m, 1H), 6.87 to 6.67 (m, 2H), 6.61 (d, J = 7.8 Hz, 1H), 4.58 (d, J = 16.2 Hz, 1H), 4.45 (s, 1H), 4.05 (d, J = 16.1 Hz, 1H), 2.90 to 2.74 (m, 1H), 2.74 to 2.58 (m, 1H), 2.58 to 2.37 (m, 1H), 2.29 (s, 3H), and 2.20 to 1.68 (m, 5H). ^{13}C NMR (75 MHz, MeOD) δ 161.50, 149.84 (2C), 146.87, 135.89 (2C), 133.64 (2C), 128.85, 128.26, 127.77 (2C), 125.66, 123.49, 118.36 (2C), 107.13, 51.70, 51.26, 45.21, 44.71, 44.67, 35.75, 30.78, and 20.12. ESI-MS *m/z* $[M + H]^+$ 468, 470 (3:1 ratio).

5-((2-(3-Chlorophenyl)-1′-methylspiro[indoline-3,4′-piperidin]-1-yl) methyl)-N-hydroxythiophene-2-carboxamide (NF2889)

Following the same procedure described for compound NF2886, the title compound NF2889 was obtained starting from **8b**, after purification by silica gel column chromatography (DCM/MeOH/NH_4OH 10:1:0.1) as an off-white solid (24 mg, 58% yield). ^{1}H NMR (300 MHz, MeOD) δ 7.50 to 7.05 (m, 7H), 6.92 to 6.70 (m, 2H), 6.63 (br, 1H), 4.59 (d, J = 16.2 Hz, 1H), 4.45 (s, 1H), 4.08 (d, J = 16.2 Hz, 1H), 2.99 to 2.81 (m, 1H), 2.83 to 2.63 (m, 1H), 2.64 to 2.43 (m, 1H), 2.34 (s, 3H),

and 2.25 to 1.70 (m, 5H). ^{13}C NMR (75 MHz, MeOD) δ 161.5, 149.8, 146.9, 139.4, 135.6, 134.6, 129.8 (2C), 128.5, 127.9 (2C), 127.1, 125.7, 123.5, 118.5 (2C), 107.3, 76.1, 51.6, 51.2, 45.2, 44.8, 44.3, 30.6, and 29.4. ESI-MS *m/z* $[M + H]^+$ 468, 470 (3:1 ratio)

Reagents

Chemicals and molecular biology reagents if not otherwise stated were purchased from Sigma–Aldrich or Thermo Fisher Scientific; talon superflow histidine-tagged protein purification resin from GE Healthcare Life Sciences; CellTiter-Glo reagent from Promega; Dulbecco's modified Eagle's medium (DMEM) with or without phenol red, Hepes, l-glutamine from Lonza; the primary monoclonal anti-α-tubulin antibody (DM1A) from Sigma–Aldrich; the antiacetylated-lysine (Ac-K2-100) from Cell Signaling Technology; the goat antimouse and anti-rabbit IgG (H + L) horseradish peroxidase secondary antibodies from Bio-Rad Laboratories. Fluor De Lys HDAC8 Fluorimetric Drug Discovery Kit (BML-AK518) was from Enzo Life Science.

Ethics statement

Animal work was approved by the National Research Council, Institute of Biochemistry and Cell Biology Animal Welfare Committee (OPBA) and by the competent authorities of the Italian Ministry of Health, DGSAF, Rome (authorization nos. 25/2014-PR and 336/2018-PR). All experiments were conducted in respect to the 3R rules according to the ethical and safety rules and guidelines for the use of animals in biomedical research provided by the relevant Italian law and European Union Directive (Italian Legislative Decree 26/2014 and 2010/63/EU) and the International Guiding Principles for Biomedical Research Involving Animals (Council for the International Organizations of Medical Sciences, Geneva, Switzerland).

Life cycle S. mansoni *maintenance and viability assays*

A Puerto Rican strain of *S. mansoni* was maintained by cycling within albino *Biomphalaria glabrata*, as the intermediate host, and ICR (CD-1) outbred female mice as the definitive host, as previously described (12). Schistosomula obtained by mechanical transformation of cercariae and Percoll gradient was used for the ATP-based luminescence viability assay that we developed and validated with the CellTiterGlo (12, 13). Briefly, the schistosomula (150/well) were incubated in DMEM medium (w/o phenol red) with compounds dissolved in DMSO for 72 h, 37 °C in 5% CO_2, in 96-well black plates. Then, 50 μl/well of CellTiterGLO reagent was added and the relative luminescence unit signal was recorded after 30 min with Varioskan Lux. Data analysis was achieved using GraphPad Prism v 7.0 software (GraphPad Software Inc) and LD_{50} was obtained after nonlinear regression curve fitting, according to log (inhibitor) *versus* normalized response with a variable slope curve model.

Viability assays on adult worm pairs were based on a phenotyping scoring assessment as previously described (12, 14). Briefly, five adult pairs were incubated with selected compounds in 3 ml of DMEM complete medium. For each compound, three experiments were performed and compounds were given to parasites only once without medium addition and/or replacement. DMSO (vehicle)-treated worms were used as control samples. Viability was monitored daily under a Leica Model MZ12 stereomicroscope for 7 days and viability scores (0–3) were assigned. In particular, the following scoring criteria were adopted: 3, denoting plate-attached, good movements, clear; 2, representing slower or diminished movements, darkening, minor tegumental damage; 1, denoting movements heavily lowered, darkening, tegument heavily damaged; and 0, meaning dead, lack of any movement. For each sample, the total score was determined by the ratio of the sum of worm scores for the total number of worms (12, 14).

Western blot analysis

Ten adult pairs were treated with selected HDAC inhibitors for 24 h or 72 h. Compound concentrations were selected based on the viability curve, TSA, a pan-HDAC inhibitor, and NF264 previously described (11) were used as positive controls in the experiments; DMSO (vehicle) was the negative control. Parasites were processed as previously described (36) with the addition of 5 mM sodium butyrate in the lysis buffer and samples were analyzed by 15% SDS-PAGE, and immunoblotting was performed using α-tubulin DM1A (1:5000) or α-acetylated-lysine (1:4000) antibodies. A Chemidoc XRS Bio-Rad with a chemiluminescent camera and Bio-Rad ImageLab 4.0 software were used for the acquisition and analysis of images. Each Western blot analysis was calibrated by Ponceau staining. For densitometric analysis, bands representing acetylated lysine were adjusted to tubulin intensity and normalized to those of negative control, DMSO-treated samples.

Mutagenesis, protein purification, and HDAC8 activity assay

The W198A mutation was introduced into the *Sm*HDAC8-His6-pET-52b construct previously described (11) using the Quickchange site-directed mutagenesis kit (Agilent Technologies, Inc) and the following forward 5′-gtaactacacgaggactatacgcgaaagcttcttctactccatc-3′ and reverse 5′-gatggagtagaagaagctttcgcgtatagtcctcgtgtagttac-3′ primers; the mutation was confirmed by plasmid DNA sequencing. The construct was expressed in BL21(DE3) *Escherichia coli* cells. *Sm*HDAC8 and *Sm*HDAC8 W198A proteins were produced and purified as previously described (11). Recombinant human HDAC8 was part of the Fluor-de-Lys HDAC8 fluorimetric drug discovery kit (Enzo Life Sciences, No. BMLAK518). Dose-response curves were built for each inhibitor in order to estimate the respective IC_{50}. DMSO concentration was kept constant to 0.5%, and for each compound, a control curve (enzymes incubated with DMSO only) was added. The Fluor-de-Lys substrate, an acetylated tetrapeptide covalently linked to 4-aminomethylcoumarin (K_{ac}-H-K_{ac}-K_{ac}-AMC), was used at 50 μM. The enzyme (1.6 μM) and the compounds were allowed to equilibrate for 15 min before adding the substrate.

Hence, the reaction (performed in the 50 mM Tris–HCl, pH 8.0, 137 mM NaCl, 2.7 mM KCl, 1 mM $MgCl_2$, 10% PEG (average molecular weight 8000 Da) was allowed to proceed for 1 h at 30 °C; 2 μM TSA in 50 μl of 1× Enzo Developer II (in 50 mM Tris–HCl, pH 8.0, 137 mM NaCl, 2.7 mM KCl, 1 mM $MgCl_2$ buffer) was added to quench the reaction, then the mixture was further incubated for 1 h at 30 °C. Fluorescence was measured in a plate reader (Varioskan Lux, Thermo Fisher Scientific) with excitation wavelength at 370 nm and emission at 450 nm. Data were analyzed by nonlinear regression fit using a generalized form of a dose-response curve with GNU/Octave (GNU/Octave, version 5.2.0 John W. Eaton, David Bateman, Søren Hauberg, Rik Wehbring (2020)).

Crystallization, data collection, and reduction; phasing and structure refinement; visualization and structure analysis

Crystals of *Sm*HDAC8 were obtained at 4 °C by vapor diffusion, hanging-drop method, by mixing equal amounts of 2 to 3 mg/ml protein solution (10 mM Tris–HCl, pH 8.0, 50 mM KCl, 2 mM DTT) and well solution (21% PEG 3350, 200 mM Na/K-tartrate, pH 8.0); crystals appeared in 2 weeks. Crystals in complex with NF2624, NF2886, NF2883, NF2889, or DMSO were obtained by soaking preformed crystals with each compound to a final concentration of 20 mM, 20 mM, 50 mM, and 10 mM, respectively, dissolved in 100% DMSO or 1 μl of DMSO. The concentration of DMSO in the soaking experiments was kept under 20%. The two liquid phases freely equilibrated for 1 week; hence, crystals were harvested and placed in a cryoprotectant solution containing 21% PEG 3350, 200 mM Na/K-tartrate and either (i) 20% glycerol, 5% PEG 200, or (ii) 15% methyl-pentanediol before snap-freezing in liquid nitrogen. Data collection was performed by rotation method at 1 Å wavelength at XRD2 beamline, ELETTRA synchrotron (Trieste, Italy).

All crystals of *Sm*HDAC8 in complex with NF2624, NF2883, NF2889, and DMSO belong to the $P4_12_12$ space group, best of them diffracted up to 1.8 Å (Supporting information S1). Data reduction and scaling were performed using XDS (37) and Aimless through the ccp4i suite interface (38). Phasing was performed by molecular replacement using a deposited enzyme structure (PDB entry 4bz5) as a template for Phaser (39). Later, model building and refinement were performed by manual editing the structure using Coot (40), and Refmac5 (41) and/or Phenix/REFINE (42), respectively. Routinely, the correct placement of inhibitors was double checked by computing Polder maps by means of Phenix (43). Validation was performed by using the wwPDB validation service (https://validate-rcsb.wwpdb.org/) and Procheck (44).

Crystals of *Sm*HDAC8 in complex with NF2886 belonging to the twinned C2 space group diffracted up to 2.3 Å. Diffraction data analysis and reduction were performed using XDS (37), Scala (45), and Combat through the ccp4i suite interface (38). Both Scala (45) and Phenix/Xtriage (42) suggested that the crystal was (pseudo) merohedrally twinned, likely due to the nearly matching length of the **a** and **b** axis (see Supporting Information S1 for details). Phasing was performed by molecular replacement using the already available structure PDB entry 4bz5 and Phaser (39). Twinning was taken into account during reciprocal space refinement steps using Refmac5, which automatically managed reflections as belonging to tetartohedral twinning, with domains' fractions refined tool 0.480 (h, k, l) 0.189 (-k, -h, -l), 0.171 (k, h, -l), and 0.160 (h,-k,-l). Cycles of model building and refinement were performed by manual editing of the structure using Coot (40) and reciprocal space refinement using Refmac5 with the twin-refinement option turned on. Occasionally, real space refinement was automatically performed using Phenix/REFINE. Validation was performed by using the wwPDB validation service and Molprobity (46). The correctness of the space group assignment was double checked by Zanuda (47). Routinely, the correct placement of inhibitors was double checked by computing Polder maps by means of Phenix (43). Visualization and analysis of binding poses were performed by PyMol (The PyMOL Molecular Graphics System, Version 2.3, Schrödinger, LLC) and Coot. The Protein Contact Atlas web tool was used to get information about contacts of any compound within each structure. Structural analysis was performed by means of the Bio3d package, within R (35). Briefly, PCA was conducted using sequence alignment of 7P0Z, 7P2S, 7P2T, 7P2U, and 7P2V performed by MUSCLE (48) followed by best-fit structural superposition by Kabsch algorithm (49).

Fluorescence spectra measurement and binding

Fluorescence spectra were recorded at 25 °C on a Jasco FP-8200 spectrofluorometer equipped with a thermostat. Four to five accumulations were used to average the emission signal. *Sm*HDAC8 recombinant proteins (0.125 μM) in buffer 10 mM Tris, pH 8.0, 150 mM KCl, and 5 mM DTT were incubated 15 min at 25 °C with inhibitors (25 μM) before the measurement. The DMSO-containing sample was always included as a reference for the unbound enzyme. Control samples containing all reagents but enzymes were added to ensure that neither NF2886 nor NF2889 did emit in the same experimental conditions. All measurements were performed, recovering emission between 310 and 410, after excitation at 280 nm and 298 nm.

Binding of inhibitors to *Sm*HDAC8 were investigated by quenching of intrinsic fluorescence at 340 nm after excitation at 280 nm. Spectra were recorded at 25 °C on a Jasco FP-8200 spectrofluorometer equipped with a thermostat. Four to five accumulations were used to average the emission signal. Inhibitor concentrations ranged from 1.6 nM to 125 μM. After addition of each concentration of inhibitor the system was left free to equilibrate for 5 min under stirring at 25 °C. Dissociation constant, K_i, was obtained from nonlinear regression fit to the quadratic general equation, assuming the formation of 1:1 complex (50), as follows,

$$y = \frac{[E]+[L]_i+K_i-\sqrt{\left([E]+[L]_i+K_i\right)^2-4[E][L]_i}}{2[E]}, y = \frac{F_{max}-F_i}{F_{max}-F_{min}},$$

where F_i is the measured fluorescence after i-th ligand addition, F_{max} is the intrinsic protein fluorescence in absence of

inhibitor, F_{min} the fluorescence of the fully complexed protein, K_i the dissociation constant for the inhibitor, [E] the concentration of protein (0.125 μM, in buffer 50 mM Tris, pH 8.0, 150 mM KCl, 100 μM DTT), and $[L]_i$ the concentration of added ligand at i-th step.

Steady-state enzyme kinetics

The steady-state kinetic studies for the *Sm*HDAC8-catalyzed reaction were performed using variable concentrations of Fluor-de-Lys (Enzo LifeScience) as a fluorogenic substrate, following a method already described (51, 52) with modifications. Briefly, variable concentrations of substrate were incubated with 0.425 μM of enzyme solution in a reaction buffer (50 mM Tris–HCl, pH 8.0, 137 mM NaCl, 2.7 mM KCl, 1 mM $MgCl_2$, 10% PEG (average molecular weight 8000 Da), 1 mg/ml bovine serum albumin) at 30 °C; at fixed time points, aliquots were quenched with an equal amount of 2 μM TSA and 2 mg/ml trypsin in 50 mM Tris–HCl, pH 8.0, 137 mM NaCl, 2.7 mM KCl, and 1 mM $MgCl_2$ buffer in order to release the fluorogenic product from the deacetylated substrate. For each substrate concentration, the initial rate of the *Sm*HDAC8-catalyzed reaction was determined from the slope resulting from the fluorescence of the product *versus* time. To calculate HDAC8 activity, measurements were converted into product formation using the Fluor-de-Lys standard curve (Enzo LifeScience). Enzyme solutions were generated by incubating the enzyme with DMSO, 5 μM NF2886, or 1 μM NF2889 for 15 min at 25 °C in a thermomixer. Inhibitor concentrations were based on the IC_{50} (Table 1), in order to keep [EI]/[E_{tot}] (the ratio of enzyme bound to inhibitor *versus* total enzyme) about 0.6, assuming that IC_{50} was comparable to K_i. Nonlinear regression curves fit to the Michaelis–Menten equation were used to determine steady-state parameters (Table 3). Steady-state kinetics for hHDAC8 was performed using the commercially available enzyme (Enzo LifeScience).

Phylogeny of HDAC8 from animals' parasites

Sequences were retrieved from Ensembl Metazoa (https://metazoa.ensembl.org/index.html, release 50) and WormBase-Parasites (https://parasite.wormbase.org/index.html, release 16) web sites, using *Sm*HDAC8 as a template (entry Smp_091990). The sequences of orthologs were manually polished by discarding: (i) duplicate sequences; (ii) sequences not starting with Met; (iii) sequences which, after initial alignment with MAFFT (52), did not contain specific residues responsible for deacetylase activity (corresponding to residues D186, H188 or D285 in the Smp_091990 sequence). Hence, PRANK was used to perform the final alignment (53); the final alignment file is available upon request. IQTREE was then used to perform phylogenetic tree inference using LG as substituting model coupled to a gamma distribution for the estimation of rates across sites, four categories to approximate gamma distribution, and optimization of estimation of invariant sites (54). The best-fit model was chosen according to the Bayesian Information Criterion by using the internal routine of IQTREE. Visualization of the inferred tree was performed using FigTree software (online available http://tree.bio.ed.ac.uk/software/figtree/).

Data availability

The atomic coordinates and crystallographic structure factors for *Sm*HDAC8 complexes with the inhibitors NF2624, NF2883, NF2886, NF2889, and DMSO-bound have been deposited in the Protein Data Bank (https://www.rcsb.org) with accession codes 7P2S, 7P2T, 7P2U, 7P2V, and 7POZ, respectively.

Supporting information—This article contains supporting information (15–20, 35, 43, 48, 55, 56).

Acknowledgments—We wish to thank ELETTRA synchrotron (Basovizza, Trieste, Italy) to grant access to the facility (proposals 20190649 & 20200498); ELETTRA XRD1 and XRD2 synchrotron beamlines support team Nicola Demitri, Maurizio Polentarutti, Alberto Cassetta and Annie Heroux; Francesco Angelucci for valuable advices about protein crystallization; Andrea Bellelli for critical reading of the manuscript and stimulating discussions; Giuseppe Tocchini-Valentini for his support on protein purification; Amina Antonacci for technical support; Valentina Fustaino for her support in the PCA analysis. Special thanks are due to Stefania Colantoni for mouse husbandry and Pierluigi Palozzo for dishwashing lab technical support at IBBC-CNR.

Author contributions—F. S. and G. R. conceptualization; F. S. software; F. S. formal analysis; F. S., R. G., A. G., G. P., M. G., V. S., L. P., Stefania Butini, Simone Brogi, and G. R. investigation; G. R. resources; F. S. and G. R. data curation; F. S. and G. R. writing–original draft; F. S. , S. G., G. C., and G. R. writing–review & editing; F. S. and G. R. visualization; S. G., G. C., and G. R. supervision; G. C. and G. R. funding acquisition.

Funding and additional information—This work was supported by Ministero dell' Università e della Ricerca (MUR) (PRIN Project No. 20154JRJPP to G. C. and G. R.); CNR (National Research Council)-CNCCS (Collezione Nazionale di Composti Chimici e Centro di Screening) "Rare, Neglected and Poverty Related Diseases Schisto-discovery Project" (DSB.AD011.001.003 to G. R.), Lazio Innova POR FESR Lazio 2014 to 2020 HDACiPLAT Project (grant number A0375-2020-36575 to G. R.). R. G. was the recipient of a post-doctoral fellowship from MUR-PRIN and CNR-CNCCS grants.

Conflict of interest—The authors declare that they have no conflicts of interest with the contents of this article.

Abbreviations—The abbreviations used are: DMSO, dimethyl sulfoxide; ESI-MS, electrospray ionization-mass spectrometry; PC, principal component; PCA, principal component analysis; PDB, Protein Data Bank; PZQ, praziquantel; spp, species; TSA, Trichostatin A.

References

1. McManus, D. P., Dunne, D. W., Sacko, M., Utzinger, J., Vennervald, B. J., and Zhou, X. N. (2018) Schistosomiasis. *Nat. Rev. Dis. Prim.* **4**, 1–19
2. Cioli, D., Pica-Mattoccia, L., Basso, A., and Guidi, A. (2014) Schistosomiasis control: praziquantel forever? *Mol. Biochem. Parasitol.* **195**, 23–29

3. Leger, E., and Webster, J. P. (2017) Hybridizations within the genus schistosoma: implications for evolution, epidemiology and control. *Parasitology* **144**, 65–80
4. Hailu, G. S., Robaa, D., Forgione, M., Sippl, W., Rotili, D., and Mai, A. (2017) Lysine deacetylase inhibitors in parasites: past, present, and future perspectives. *J. Med. Chem.* **60**, 4780–4804
5. Oger, F., Dubois, F., Caby, S., Noël, C., Cornette, J., Bertin, B., *et al.* (2008) The class I histone deacetylases of the platyhelminth parasite *Schistosoma mansoni*. *Biochem. Biophys. Res. Commun.* **377**, 1079–1084
6. Nakagawa, M., Oda, Y., Eguchi, T., Aishima, S., Yao, T., Hosoi, F., *et al.* (2007) Expression profile of class I histone deacetylases in human cancer tissues. *Oncol. Rep.* **18**, 769–774
7. Millard, C. J., Watson, P. J., Fairall, L., and Schwabe, J. W. R. (2017) Targeting class I histone deacetylases in a "complex" environment. *Trends Pharmacol. Sci.* **38**, 363–377
8. Osko, J. D., Porter, N. J., Decroos, C., Lee, M. S., Watson, P. R., Raible, S. E., *et al.* (2021) Structural analysis of histone deacetylase 8 mutants associated with Cornelia de Lange Syndrome spectrum disorders. *J. Struct. Biol.* **213**, 107681
9. Werbeck, N. D., Shukla, V. K., Kunze, M. B. A., Yalinca, H., Pritchard, R. B., Siemons, L., *et al.* (2020) A distal regulatory region of a class I human histone deacetylase. *Nat. Commun.* **11**, 3841
10. Ghazy, E., Abdelsalam, M., Robaa, D., Pierce, R. J., and Sippl, W. (2022) Histone deacetylase (HDAC) inhibitors for the treatment of schistosomiasis. *Pharmaceuticals* **15**, 80
11. Saccoccia, F., Brindisi, M., Gimmelli, R., Relitti, N., Guidi, A., Saraswati, A. P., *et al.* (2020) Screening and phenotypical characterization of *Schistosoma mansoni* Histone Deacetylase 8 (SmHDAC8) inhibitors as multistage antischistosomal agents. *ACS Infect. Dis.* **6**, 100–113
12. Lalli, C., Guidi, A., Gennari, N., Altamura, S., Bresciani, A., and Ruberti, G. (2015) Development and validation of a luminescence-based, medium-throughput assay for drug screening in *Schistosoma mansoni*. *PLoS Negl. Trop. Dis.* **9**, 1–16
13. Guidi, A., Gimmelli, R., Bresciani, A., and Ruberti, G. (2020) Luminescence-based, low- and medium-throughput assays for drug screening in Schistosoma mansoni larval stage. *Met. Mol. Biol.* **2151**, 219–227
14. Guidi, A., Lalli, C., Gimmelli, R., Nizi, E., Andreini, M., Gennari, N., *et al.* (2017) Discovery by organism based high-throughput screening of new multi-stage compounds affecting *Schistosoma mansoni* viability, egg formation and production. *PLoS Negl. Trop. Dis.* **11**, e0005994
15. Marek, M., Kannan, S., Hauser, A. T., Moraes Mourão, M., Caby, S., Cura, V., *et al.* (2013) Structural basis for the inhibition of Histone Deacetylase 8 (HDAC8), a key epigenetic player in the blood fluke *Schistosoma mansoni*. *PLoS Pathog.* **9**, e1003645
16. Bayer, T., Chakrabarti, A., Lancelot, J., Shaik, T. B., Hausmann, K., Melesina, J., *et al.* (2018) Synthesis, crystallization studies, and *in vitro* characterization of cinnamic acid derivatives as SmHDAC8 inhibitors for the treatment of Schistosomiasis. *ChemMedChem* **13**, 1517–1529
17. Marek, M., Shaik, T. B., Heimburg, T., Chakrabarti, A., Lancelot, J., Ramos-Morales, E., *et al.* (2018) Characterization of Histone Deacetylase 8 (HDAC8) selective inhibition reveals specific active site structural and functional determinants. *J. Med. Chem.* **61**, 10000–10016
18. Simoben, C. V., Robaa, D., Chakrabarti, A., Schmidtkunz, K., Marek, M., Lancelot, J., *et al.* (2018) A novel class of *Schistosoma mansoni* histone deacetylase 8 (HDAC8) inhibitors identified by structure-based virtual screening and *in vitro* testing. *Molecules* **23**, 566
19. Stolfa, D. A., Marek, M., Lancelot, J., Hauser, A. T., Walter, A., Leproult, E., *et al.* (2014) Molecular basis for the antiparasitic activity of a mercaptoacetamide derivative that inhibits Histone Deacetylase 8 (HDAC8) from the human pathogen. *Schistosoma Mansoni. J. Mol. Biol.* **426**, 3442–3453
20. Ghazy, E., Heimburg, T., Lancelot, J., Zeyen, P., Schmidtkunz, K., Truhn, A., *et al.* (2021) Synthesis, structure-activity relationships, cocrystallization and cellular characterization of novel smHDAC8 inhibitors for the treatment of schistosomiasis. *Eur. J. Med. Chem.* **225**, 113745
21. Palmer, T. (1985) *Understanding Enzymes*, 2nd Ed., Ellis Horwood Publishers, Market Cross House, Cooper Street, Chichester
22. Wharton, C. W., and Eisenthal, R. (1981) *Molecular Enzymology*, 1st Ed., Blackie & Son, Bishopbriggs, Glasgow
23. Dubois, F., Caby, S., Oger, F., Cosseau, C., Capron, M., Grunau, C., *et al.* (2009) Histone deacetylase inhibitors induce apoptosis, histone hyperacetylation and up-regulation of gene transcription in *Schistosoma mansoni*. *Mol. Biochem. Parasitol.* **168**, 7–15
24. Pierce, R. J., Dubois-Abdesselem, F., Caby, S., Trolet, J., Lancelot, J., Oger, F., *et al.* (2011) Chromatin regulation in schistosomes and histone modifying enzymes as drug targets. *Mem. Inst. Oswaldo Cruz* **106**, 794–801
25. Su, H., Altucci, L., and You, Q. (2008) Competitive or noncompetitive, that's the question: research toward histone deacetylase inhibitors. *Mol. Cancer Ther.* **7**, 1007–1012
26. Copeland, R. A. (2013) *Evaluation of Enzyme Inhibitors in Drug Discovery: A Guide for Medicinal Chemists and Pharmacologists*, 1st Ed., Wiley
27. Bellelli, A., and Carey, J. (2018) *Reversible Ligand Binding*. Wiley
28. Buker, S. M., Boriack-Sjodin, P. A., and Copeland, R. A. (2019) Enzyme-inhibitor interactions and a Simple, rapid method for determining inhibition modality. *SLAS Discov.* **24**, 515–522
29. Zhou, J., Huang, Y., Cheng, C., Wang, K., and Wu, R. (2017) Intrinsic dynamics of the binding rail and its allosteric effect in the class I histone deacetylases. *J. Chem. Inf. Model.* **57**, 2309–2320
30. Shukla, V. K., Siemons, L., Gervasio, F. L., and Hansen, D. F. (2021) Aromatic side-chain flips orchestrate the conformational sampling of functional loops in human histone deacetylase 8. *Chem. Sci.* **12**, 9318–9327
31. Amadei, A., Linssen, A. B., and Berendsen, H. J. (1993) Essential dynamics of proteins. *Proteins* **17**, 412–425
32. Skjaerven, L., Grant, B., Muga, A., Teigen, K., McCammon, J. A., Reuter, N., *et al.* (2011) Conformational sampling and nucleotide-dependent transitions of the GroEL subunit probed by unbiased molecular dynamics simulations. *PLoS Comput. Biol.* **7**, e1002004
33. Yao, X., and Grant, B. J. (2013) Domain-opening and dynamic coupling in the α-subunit of heterotrimeric G proteins. *Biophys. J.* **105**, L08–L10
34. Stiers, K. M., Graham, A. C., Zhu, J., Jakeman, D. L., and Nix, J. C. (2019) Structural and dynamical description of the enzymatic reaction of a phosphohexomutase. *Struct. Dyn.* **6**, 024703
35. Grant, B. J., Rodrigues, A. P. C., ElSawy, K. M., McCammon, J. A., and Caves, L. S. D. (2006) Bio3d: an R package for the comparative analysis of protein structures. *Bioinformatics* **22**, 2695–2696
36. Guidi, A., Saccoccia, F., Gennari, N., Gimmelli, R., Nizi, E., Lalli, C., *et al.* (2018) Identification of novel multi-stage histone deacetylase (HDAC) inhibitors that impair *Schistosoma mansoni* viability and egg production. *Parasit Vectors* **11**, 668
37. Kabsch, W. (2010) Integration, scaling, space-group assignment and post-refinement. *Acta Crystallogr. Sect. D Biol. Crystallogr.* **66**, 133–144
38. Winn, M. D., Ballard, C. C., Cowtan, K. D., Dodson, E. J., Emsley, P., Evans, P. R., *et al.* (2011) Overview of the CCP4 suite and current developments. *Acta Crystallogr. Sect. D Biol. Crystallogr.* **67**, 235–242
39. McCoy, A. J., Grosse-Kunstleve, R. W., Adams, P. D., Winn, M. D., Storoni, L. C., and Read, R. J. (2007) Phaser crystallographic software. *J. Appl. Crystallogr.* **40**, 658–674
40. Emsley, P., Lohkamp, B., Scott, W. G., and Cowtan, K. (2010) Features and development of Coot. *Acta Crystallogr. Sect. D Biol. Crystallogr.* **66**, 486–501
41. Murshudov, G. N., Vagin, A. A., and Dodson, E. J. (1997) Refinement of macromolecular structures by the maximum-likelihood method. *Acta Crystallogr. Sect. D Biol. Crystallogr.* **53**, 240–255
42. Liebschner, D., Afonine, P. V., Baker, M. L., Bunkóczi, G., Chen, V. B., Croll, T. I., *et al.* (2019) Macromolecular structure determination using X-rays, neutrons and electrons: recent developments in Phenix. *Acta Crystallogr. Sect. D Struct. Biol.* **75**, 861–877
43. Sobolev, O. V., Terwilliger, C., and Adams, P. D. (2017) Polder maps: Improving OMIT maps by excluding bulk solvent. *Acta Crystallogr. Sect. D Biol. Crystallogr.* **73**, 148–157
44. Laskowski, R. A., MacArthur, M. W., Moss, D. S., and Thornton, J. M. (1993) PROCHECK: a program to check the stereochemical quality of protein structures. *J. Appl. Crystallogr.* **26**, 283–291
45. Evans, P. (2006) Scaling and assessment of data quality. *Acta Crystallogr. Sect. D Biol. Crystallogr.* **62**, 72–82

46. Williams, C. J., Headd, J. J., Moriarty, N. W., Prisant, M. G., Videau, L. L., Deis, L. N., *et al.* (2018) MolProbity: more and better reference data for improved all-atom structure validation. *Protein Sci.* **27**, 293–315
47. Lebedev, A. A., and Isupov, M. N. (2014) Space-group and origin ambiguity in macromolecular structures with pseudo-symmetry and its treatment with the program Zanuda. *Acta Crystallogr. Sect. D Biol. Crystallogr.* **70**, 2430–2443
48. Edgar, R. C. (2004) MUSCLE: a multiple sequence alignment method with reduced time and space complexity. *BMC Bioinformatics* **5**, 113
49. Kabsch, W. (1978) A discussion of the solution for the best rotation to relate two sets of vectors. *Acta Crystallogr. Sect. A.* **34**, 827–828
50. van de Weert, M., and Stella, L. (2011) Fluorescence quenching and ligand binding: a critical discussion of a popular methodology. *J. Mol. Struct.* **998**, 144–150
51. Toro, T. B., and Watt, T. J. (2015) KDAC8 substrate specificity quantified by a biologically relevant, label-free deacetylation assay. *Protein Sci.* **24**, 2020–2032
52. Katoh, K., Misawa, K., Kuma, K. I., and Miyata, T. (2002) Mafft: a novel method for rapid multiple sequence alignment based on fast fourier transform. *Nucl. Acids Res.* **30**, 3059–3066
53. Löytynoja, A., and Goldman, N. (2005) An algorithm for progressive multiple alignment of sequences with insertions. *Proc. Natl. Acad. Sci. U. S. A.* **102**, 10557–10562
54. Nguyen, L. T., Schmidt, H. A., Von Haeseler, A., and Minh, B. Q. (2015) IQ-TREE: a fast and effective stochastic algorithm for estimating maximum-likelihood phylogenies. *Mol. Biol. Evol.* **32**, 268–274
55. Heimburg, T., Chakrabarti, A., Lancelot, J., Marek, M., Melesina, J., Hauser, A. T., *et al.* (2016) Structure-based design and synthesis of novel inhibitors targeting HDAC8 from *Schistosoma mansoni* for the treatment of schistosomiasis. *J. Med. Chem.* **59**, 2423–2435
56. Roversi, P., Blanc, E., Johnson, S., and Lea, S. M. (2012) Tetartohedral twinning could happen to you too. *Acta Crystallogr. D: Biol. Crystallogr.* **68**, 418–424